ARTICLE IN PRESS

Planetary and Space Science xxx (xxxx) xxx

Contents lists available at ScienceDirect

Planetary and Space Science

journal homepage: www.elsevier.com/locate/pss

Improved LOLA elevation maps for south pole landing sites: Error estimates and their impact on illumination conditions

Michael K. Barker [a,*], Erwan Mazarico [a], Gregory A. Neumann [a], David E. Smith [b], Maria T. Zuber [b], James W. Head [c]

[a] NASA Goddard Space Flight Center, Greenbelt, MD 20771, USA
[b] Department of Earth, Atmospheric, and Planetary Sciences, MIT, Cambridge, MA, 02139, USA
[c] Department of Earth, Environmental and Planetary Sciences, Brown University, Providence, RI 02912, USA

ARTICLE INFO

Keywords:
Polar illumination
Moon
Landing sites
Space exploration
LOLA

ABSTRACT

We present new high-resolution topographic models of 4 high-priority lunar south pole landing sites based exclusively on the laser altimetry data acquired by the Lunar Orbiter Laser Altimeter (LOLA) onboard the Lunar Reconnaissance Orbiter. By iteratively adjusting the LOLA tracks to the LOLA-based digital elevation model (LDEM) in a self-consistent fashion, we reduce the orbital geolocation errors by over a factor of 10 such that the new ground track geolocation uncertainty is ~10–20 cm horizontally and ~2–4 cm vertically over each 16 × 16 km region. These new and improved 5 m/pix LDEMs will be useful to constrain higher-resolution topographic models derived from imagery, which are not as well controlled geodetically and which can be hindered by shadows. We developed a method to estimate surface height uncertainty in the new LDEMs, which accounts for the reduced orbital errors and interpolation errors by assuming a fractal behavior for the short-scale topography. The LDEM surface height and slope uncertainties have typical RMS values of ~0.30–0.50 m and ~1.5–2.5°, respectively. Finally, we examine how height uncertainties propagate to variations in horizon elevation and thus the predicted illumination conditions at these polar latitudes, and we show how this error characterization can inform landing site studies.

1. Introduction

The Moon's polar regions hold great interest for both science and exploration due to its low obliquity, and the extreme lighting and temperature conditions at its poles. Permanently Shadowed Regions (PSRs) inside craters have temperatures reaching below ~100 K, making them cold traps for volatiles such as water (Watson et al., 1961; Arnold 1979; Hayne et al., 2015; Fisher et al., 2017; Li et al., 2018). These volatiles could provide critical in-situ resources for future long-term outposts, as envisioned in NASA's Artemis program and its Plan for Sustained Lunar Exploration and Development[1]. Some PSRs nearest to the poles lie within a short distance of tall peaks that are ideal locations for power and communication systems for their long periods in view of the Sun and Earth (Gläser et al., 2018). Multiple national and international public- and private-sector organizations are actively planning to send robotic and human explorers to the south pole (*e.g.,* Ivanov et al., 2015; Colaprete et al., 2020; Ohtake et al., 2020). For these reasons, it is important to have the most detailed and accurate topographic maps possible. Such maps are critical inputs to mission design studies, in particular to the identification of high-science-priority sites (Flahaut et al., 2020), planning of optimal rover traverses (Speyerer et al., 2016), and solar array height and location (Bryant et al., 2009; Mazarico et al., 2011). These studies require accurate, precise, and high-resolution maps of surface height, slope, and roughness both outside and within PSRs (De Rosa et al., 2012; Heldmann et al., 2016).

Well established techniques that use images to produce topographic models, such as stereophotogrammetry (SPG; Henriksen et al., 2017) and shape-from-shading (SfS; Alexandrov and Beyer 2018), face significant challenges in polar regions due to the extreme shadowing. Given their active ranging capabilities, laser altimeters are not hindered by shadows. However, gaps between laser ground tracks and individual laser spots necessitate interpolation and increase uncertainties in altimeter-based digital elevation models (DEMs). Addressing these uncertainties is one of the primary goals of this work.

* Corresponding author.
E-mail address: Michael.k.barker@nasa.gov (M.K. Barker).

[1] https://www.nasa.gov/sites/default/files/atoms/files/a_sustained_lunar_presence_nspc_report4220final.pdf.

https://doi.org/10.1016/j.pss.2020.105119
Received 22 April 2020; Received in revised form 30 September 2020; Accepted 14 October 2020
Available online xxxx

Please cite this article as: Barker, M.K. et al., Improved LOLA elevation maps for south pole landing sites: Error estimates and their impact on illumination conditions, Planetary and Space Science, https://doi.org/10.1016/j.pss.2020.105119

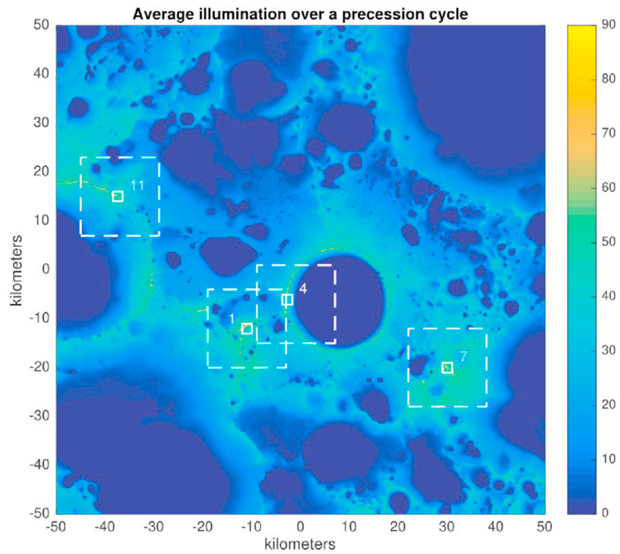

Fig. 1. Average illumination of the Sun at the lunar south pole (240 m/pix) over a full 18.6 year precession cycle. Small squares mark the 4 high-priority landing sites whose illumination conditions are studied here and boxes outline the 16 × 16 km regions for which we derive new 5 m/pix DEMs (see Figs. 2 and 3). The regions are labeled with their designated ID numbers: 1, 4, 7, and 11 following Mazarico et al. (2011). In this and all subsequent maps, the projection is stereographic centered on the south pole at the origin.

The Lunar Orbiter Laser Altimeter (LOLA) onboard the Lunar Reconnaissance Orbiter (LRO) has collected nearly 7 billion measurements of surface height producing the geodetic framework for aligning LRO (and other lunar) datasets. Though small, errors in the LRO orbit reconstruction (~7/7/0.5 m in the along-track, cross-track & radial directions, or A/C/R; Mazarico et al., 2018a) cause streaky artifacts in the LOLA DEM (LDEM) products. Isolated noise returns (~1% of total) can appear as spurious “flag-poles” or “pot-holes”. These artifacts are more apparent at higher DEM resolution, which creates a problem for landing site studies. Most such artifacts can be removed by adjusting the tracks to a reference DEM, such as those produced by SPG or SfS methods applied to LRO Narrow Angle Camera (NAC) images (Gläser et al., 2018). The reference DEM does not have to be perfect. Although the 5 m/pix LDEM contains artifacts and has data in only ~10% of pixels near the south pole, it contains enough information to act as the reference DEM for this purpose. Although nothing can improve the coverage of the LDEM (number of gaps between tracks and individual laser spots), this track adjustment process can produce a vastly cleaner LDEM with fewer artifacts. An updated 5 m/pix LDEM will be more useful for landing site studies and as a constraint to higher-resolution DEMs from SPG and SfS. A major advantage of this process is that it enables us to estimate, for the first time, realistic LDEM height uncertainties due to both orbital errors and interpolation, and their effects on illumination conditions. These uncertainties can now be quantitatively considered in mission design studies.

In this study, we apply these methods to 4 south pole locations (Fig. 1)

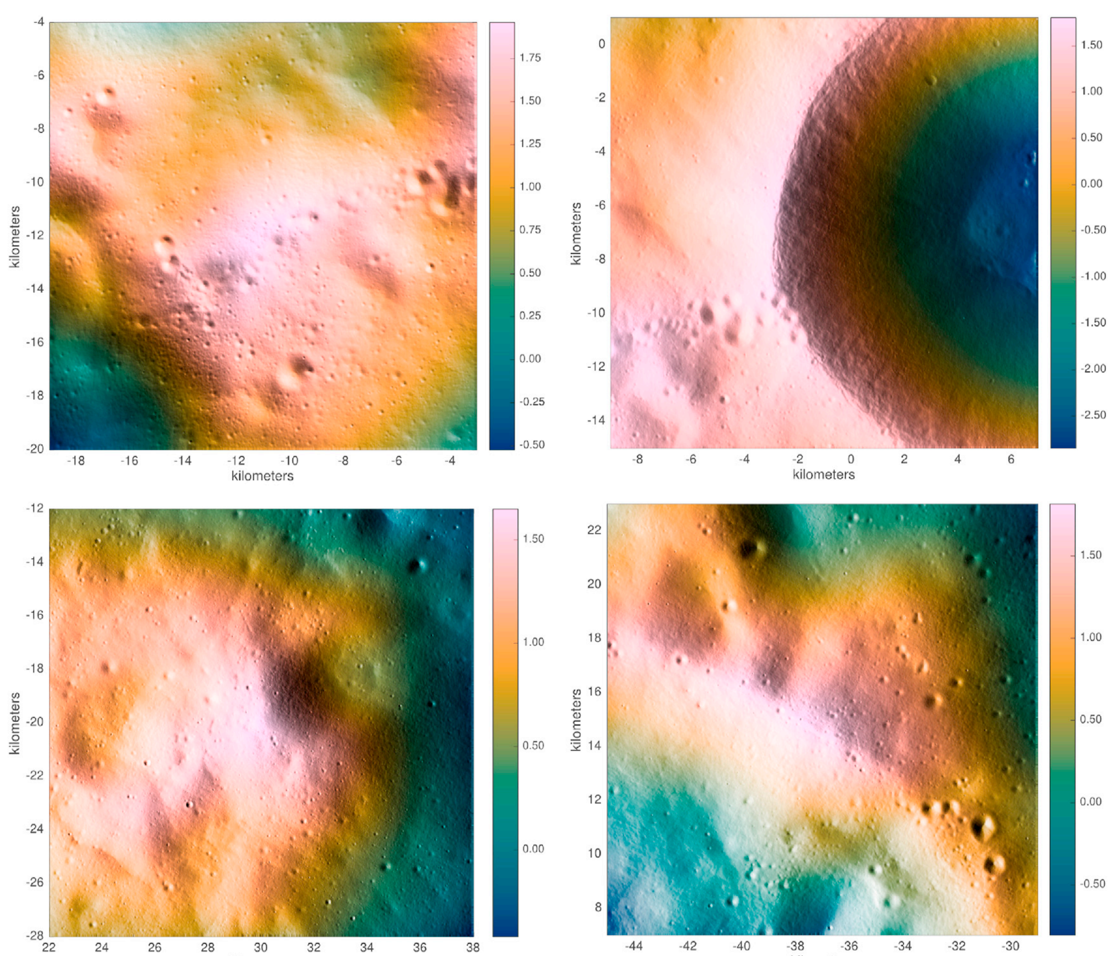

Fig. 2. Shaded relief images of the new LDEMs derived in this work for Site 1 (top-left), Site 4 (top-right), Site 7 (bottom-left), and Site 11 (bottom-right). The color scale is in km. The pixel scale is 5 m/pix and the projection is stereographic centered on the south pole at the origin. (For interpretation of the references to color in this figure legend, the reader is referred to the Web version of this article.)

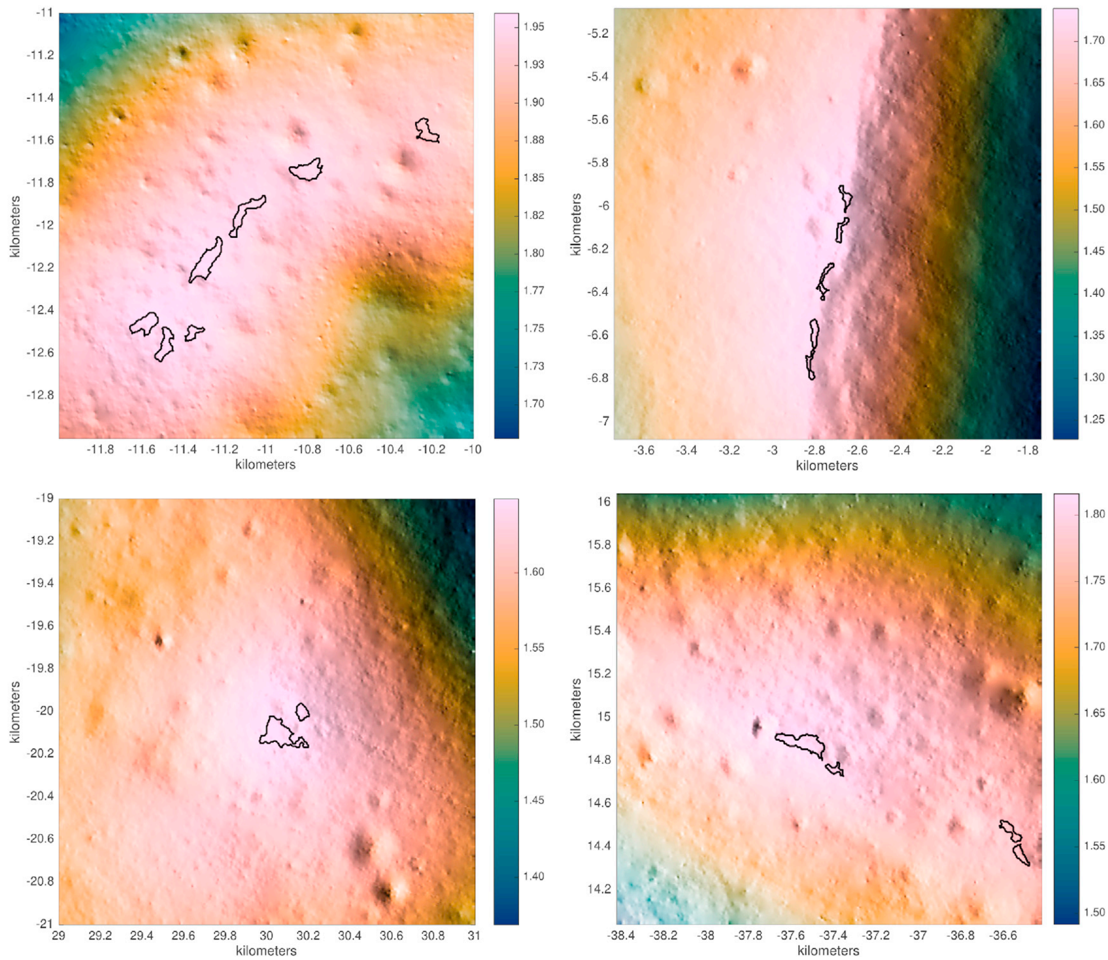

Fig. 3. 2 × 2 km close-up shaded relief images of Site 1 (top-left), Site 4 (top-right), Site 7 (bottom-left), and Site 11 (bottom-right). The color scale is in km. The pixel scale is 5 m/pix and the projection is stereographic centered on the south pole at the origin. Black lines surround regions larger than 2500 m^2 with average illumination over 70% between Jan. 1, 2024 and Jan. 1, 2026. (For interpretation of the references to color in this figure legend, the reader is referred to the Web version of this article.)

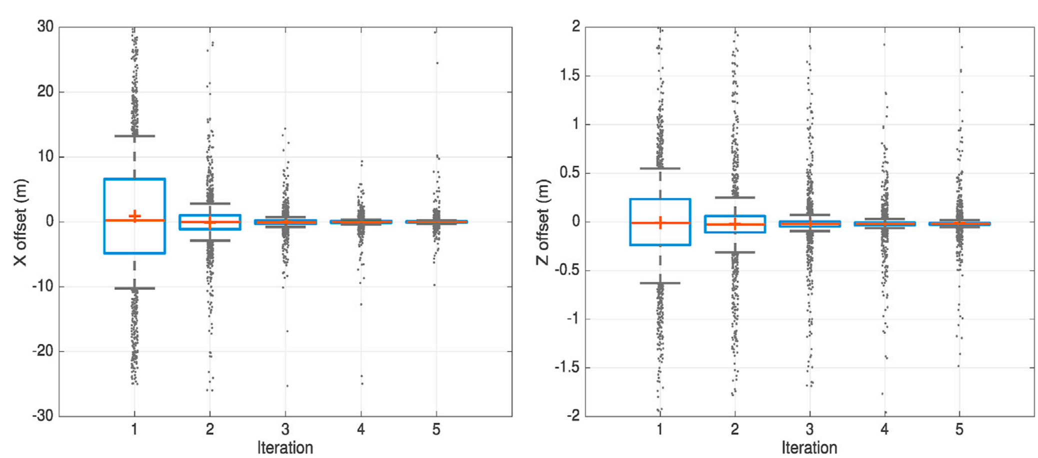

Fig. 4. Box-plots of the distribution of best-fit X and Z track offsets for each iteration of Site 1: mean (+), median (−), inter-quartile range (box), 9th/91st percentiles (whiskers), individual tracks <9% or >91% (dots). Offsets converge towards zero and their dispersion decreases with each iteration. Y offsets (not shown) are similar to X.

previously identified as good potential landing sites based on their favorable illumination conditions (Bussey et al., 1999, 2010; Fincannon 2007; Noda et al., 2008; Mazarico et al., 2011). The numbering scheme we adopt for the sites is the same as in Table3 of Mazarico et al. (2011), which ranked them according to average illumination over a full precession cycle (~18.6 years) using the 240 m/pix LDEM. Site 1 is the connecting ridge between Shackleton crater and de Gerlache crater, Site 4 is on the rim of Shackleton, Site 7 is an isolated peak near Shackleton on the far side, and Site 11 is on the rim of de Gerlache. The illumination conditions around these sites were recently studied by De Rosa et al.

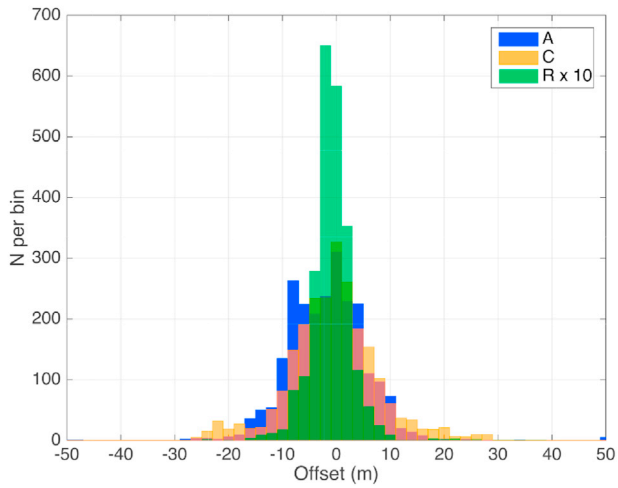

Fig. 5. Total A/C/R track offsets summed over all iterations. The median is −1.58/-0.51/-0.10 m and the MAD_b is 7.01/6.59/0.27 m, consistent with independent estimates of orbital errors.

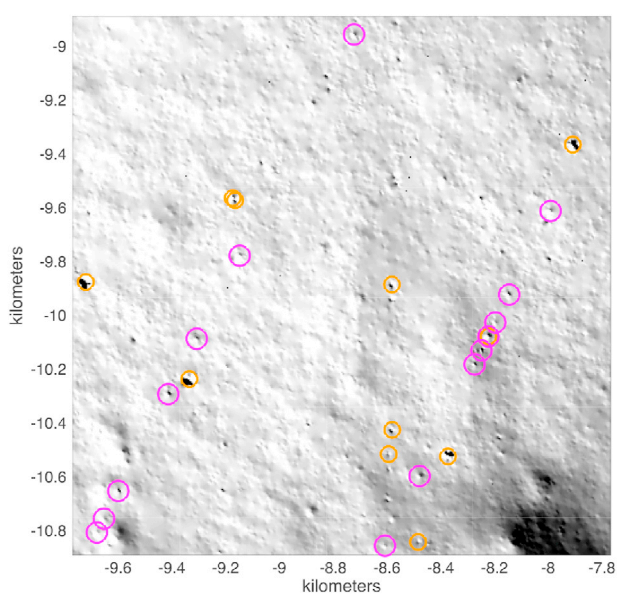

Fig. 6. Examples of points that were removed after the final iteration because they failed a slope test (orange) or they belonged to runs of large residuals (magenta). In total, ~0.1% of all the LOLA points were removed. (For interpretation of the references to color in this figure legend, the reader is referred to the Web version of this article.)

(2012) and Gläser et al. (2014; 2018). Sites 1, 4, 7, and 11 correspond, respectively, to CR1, SR1, SV1, and GR1 of De Rosa et al. (2012) and Sites 1 and 4 correspond, respectively, to C1 and S of Gläser et al. (2018). The primary differences between these previous studies and ours is that we run illumination simulations at a higher resolution (5 m/pix vs. 40 m/pix in De Rosa et al., 2012 and 20 m/pix in Gläser et al., 2014; 2018), and we perform a detailed analysis of LDEM height uncertainties and their impact on illumination conditions.

This paper is organized as follows. In Section 2, we describe the LOLA instrument and data, as well as the 4 individual regions studied here. We describe the track adjustment and cleaning process and the resulting new LDEMs in Section 3. Then, in Section 4, we develop and apply statistical methods to quantify LDEM height uncertainties. In Section 5, we perform illumination simulations to assess the impact of the LDEM height uncertainties on the illumination conditions at the 4 sites for the period Jan. 1, 2024–Jan. 1, 2026, the earliest time frame targeted by the Artemis program.

2. Instrument and data description

LOLA is a time-of-flight laser altimeter operating with a firing rate of 28 Hz and a cross-shaped, 5-spot footprint on the surface canted by 26° from the along-track direction to optimize coverage overlap (Smith et al., 2017). From commissioning in July 2009 to the start of the mapping phase in September 2009, LRO orbited in a 30 × 200 km elliptical orbit with periselene in the southern hemisphere. Subsequently, LRO entered its nominal 50-km near-circular mapping orbit, where it remained until December 2011 when it transitioned to a near-frozen elliptical orbit similar to commissioning. After this time, LOLA collected very few returns in the northern hemisphere as the spacecraft was too high for altimetric ranging. However, it did continue to collect data in the south, and the latest data we use were taken in September 2013, after which time these near-polar latitudes became inaccessible due to a natural drift in orbital inclination (Mazarico et al., 2018a). From an altitude of 50 km, the cross-track spacing between each profile is 12 m with an along-track spacing of 57 m between each measurement in a profile, and each spot footprint has a diameter of 5 m, suggesting a natural minimum pixel scale of 5 m/pix for the LDEM product, the one we use here. The range precision inherent to the LOLA timing electronics is ~10 cm, which sets an absolute floor to the vertical geolocation uncertainty of any individual laser return.

We consider the LOLA data within 16 × 16 km square regions surrounding each site. Fig. 2 shows the new LDEMs that we derive (Section 3). Note that our LDEM for Site 4 also contains Site 8 from Mazarico et al. (2011), or SR2 of De Rosa et al. (2012). Most of the results shown and discussed below focus on Site 1 whose dataset consists of ~2500 tracks with ~1 million individual returns. The results for the other sites, with at most 25% fewer returns, are similar. Fig. 3 shows 2 × 2 km close-ups of each site with black contours surrounding regions with average illumination (visible fraction of the Sun's disk) greater than 70% at a height 1 m above the surface between Jan. 1, 2024 and Jan. 1, 2026, and area >2500 m^2 (Section 5). To be consistent with the LRO project, we work entirely in the Mean Earth/Polar Axis (MOON_ME) coordinate frame of JPL ephemeris DE421 (Folkner et al., 2009). The orientation of this frame in this ephemeris has an overall uncertainty of a few meters with respect to the principal axis frame (Williams et al., 2008).

3. New LDEM methods and results

3.1. Track adjustments

Our method is based on fitting geolocated LOLA profiles to each other. First, the raw point cloud of LOLA returns is binned into 5 m pixels. Then, empty pixels in the LDEM are interpolated with the Generic Mapping Tools (GMT) continuous curvature 'surface' routine with tension parameter T = 0.75 (Smith et al., 1990; Wessel et al., 2013). This parameter can range between 0 and 1, where 0 gives the minimum curvature (bicubic) solution and 1 gives a harmonic spline solution (where local minima and maxima occur only at filled pixels). For the track adjustments, we use an iterative process, in which we randomly remove 2% of the tracks from the 5 m/pix LDEM, adjust each of the missing tracks individually to the resulting "reduced" LDEM (after a new interpolation) by applying 3-dimensional offsets in the X/Y/Z directions (i.e., stereographic map coordinates and height), and repeat until all tracks have been adjusted. By fitting each track to the reduced LDEM with that track removed, we ensure that outliers can be detected and that the track is not adjusted to itself. Only nadir-pointing tracks are included since this process would not work as well for off-nadir tracks due to topographic distortion effects. The process of running 50 batches until all tracks are adjusted is repeated 5 times in total (yielding 250 total batches), each time starting from a new LDEM computed with the best-fit

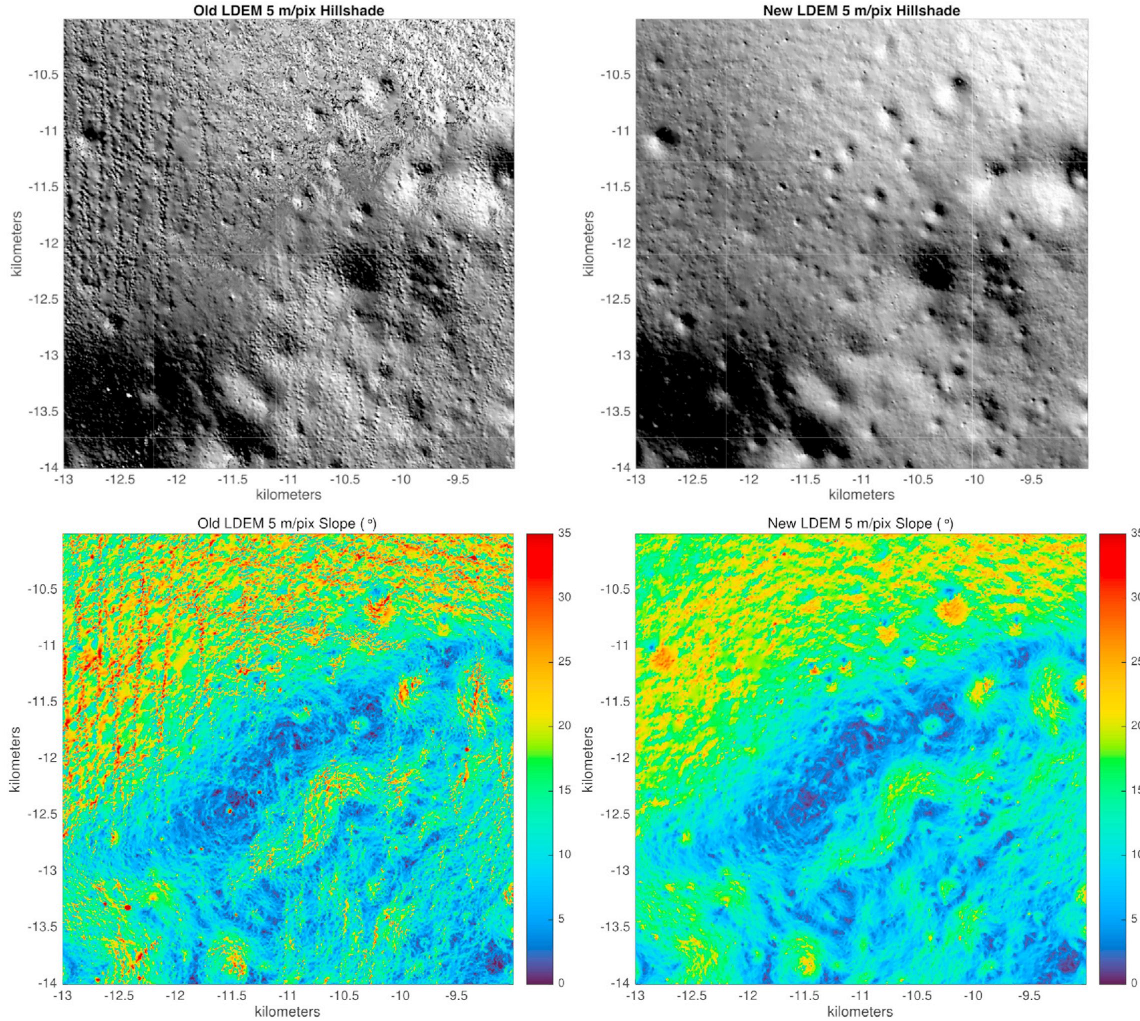

Figs. 7. 4 × 4 km close-up of Site 1 comparing the old 5 m/pix LDEM (left column) and the new LDEM that we derive (right column). The hillshade (top row) and slope map (bottom row) show how the track adjustment and cleaning process has removed the vast majority of streaky artifacts and bad points.

track adjustments from the previous iteration. Outlying points are not removed until after the final iteration, but are down-weighted during the track fitting by multiplying the residuals with a Cauchy function (Polat 2020) to ensure outliers do not bias the results. The fitting algorithm minimizes the root-mean-squared (RMS) vertical (Z) surface height residuals between each individual laser return (referred to here as a point) and the surface height at that location on the current "reduced" LDEM (built with the remaining 98% of the data).

The median of the Z residuals after the final iteration is 0.00 m. To measure the spread of Z residuals, we use the quantity, $MAD_b = 1.48 \times MAD$ where MAD is the median absolute deviation. MAD_b is often favored for its robustness to outliers and consistency as a scale estimator (*e.g.*, Huber 1981; Leys et al., 2013). In particular, for normally-distributed data, MAD_b is equal to the standard deviation. The value of MAD_b for the Z residuals is 0.42, which provides a first estimate of the typical interpolation error since each track was removed before fitting it to a "reduced" LDEM with mostly interpolated pixels where the track had been.

The track adjustments (or offsets) at each iteration converge towards zero and their dispersion decreases (Fig. 4). After 5 iterations, the median stereographic X/Y/Z offset is 0.00/0.01/-0.02 m and the MAD_b is 0.14/0.12/0.02 m and further iterations are unnecessary. The resulting final geolocation uncertainty (after the 5th iteration in Fig. 4) is thus less than ~12–14 cm horizontally and ~2 cm vertically for most (~68%) of the tracks, more than an order of magnitude improvement over the original geolocation uncertainties due to orbital errors. This geolocation uncertainty, which applies to total absolute position, is not to be confused with the uncertainty in surface height, *i.e.*, elevation above the reference sphere (see Section 4). Natural terrain slope variations and sub-pixel sampling cause the latter to be larger than the former.

The X/Y/Z offsets are transformed to the A/C/R frame using each track's unique angle of rotation with respect to the stereographic frame. The median total A/C/R track offsets summed over all iterations (Fig. 5) are −1.58/-0.51/-0.10 m and the MAD_b is 7.01/6.59/0.27 m, consistent with independent estimates of orbital errors based on reconstructed orbit overlap statistics (Mazarico et al., 2018a) and the locations of anthropogenic sites in NAC images (Wagner et al., 2017). Pointing errors are expected to make a minor contribution to the track offsets since we use only nadir tracks and the LOLA data processing pipeline applies a day/night pointing offset to account for the thermal blanket anomaly (Smith et al., 2017). Indeed, the horizontal RMS track offsets are consistent with those derived from pointing-corrected crossovers suggesting the pointing errors are minimal (Barker et al., 2018).

3.2. *Removing outliers*

After the final iteration, visual inspection of the hillshaded LDEM reveals a small percentage of outlying points: some isolated invalid LOLA returns (*e.g.*, flag poles) and runs (streaks) of a few consecutive poor-quality returns. We developed an automated process to remove these

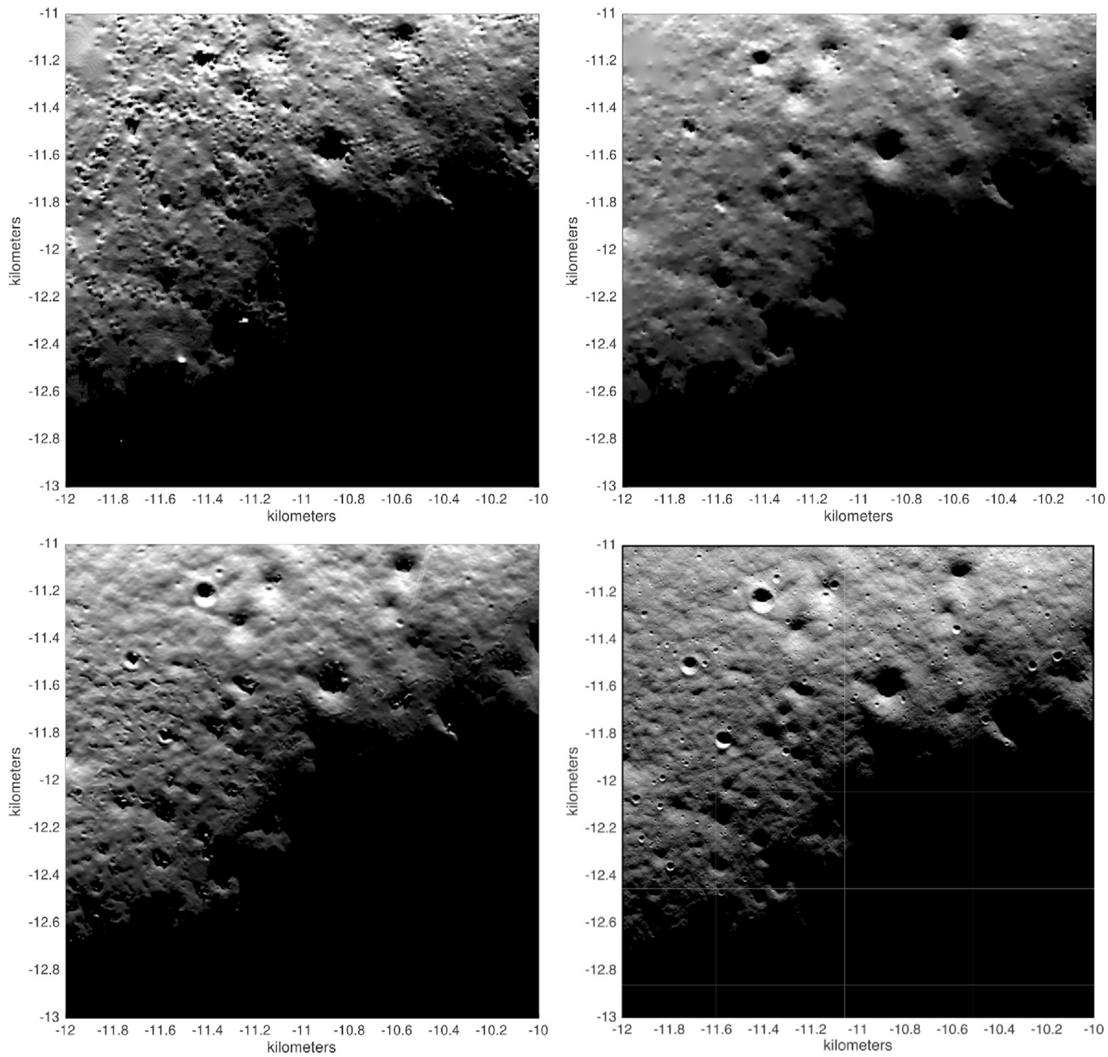

Figs. 8. 2 × 2 km simulated image of Site 1 using the old 5 m/pix LDEM (top-left), the new LDEM that we derive (top-right), and an SPG-based NAC 2 m/pix DEM (bottom-left) compared to the NAC 1 m/pix image M139811097 L/R (bottom-right).

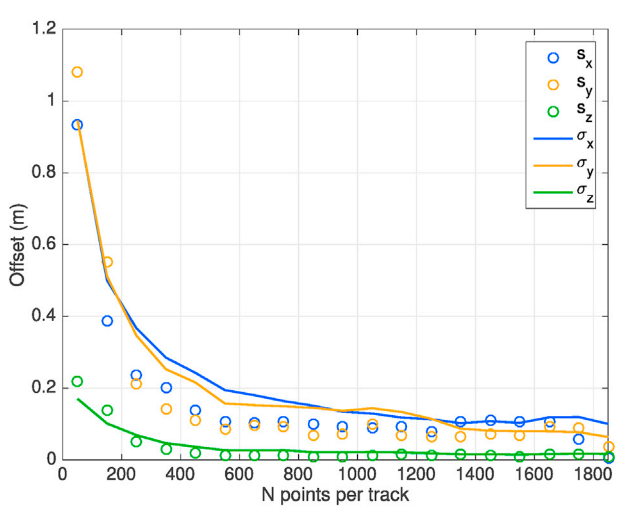

Fig. 9. Track offset uncertainties estimated from their covariance matrix and binned by number of points per track (solid lines) provide a close approximation to the standard deviation of offsets in iteration 5 (open circles).

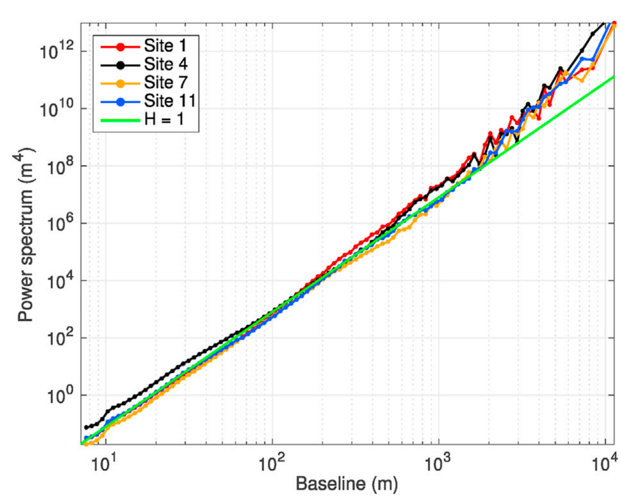

Fig. 10. Power spectra of all 4 sites (lines with points) compared to a random fractal surface with Hurst exponent H = 1 (green line). Excess power in the data on baselines ≳ 10% of the maximum is a bias introduced by undersampling the surface. (For interpretation of the references to color in this figure legend, the reader is referred to the Web version of this article.)

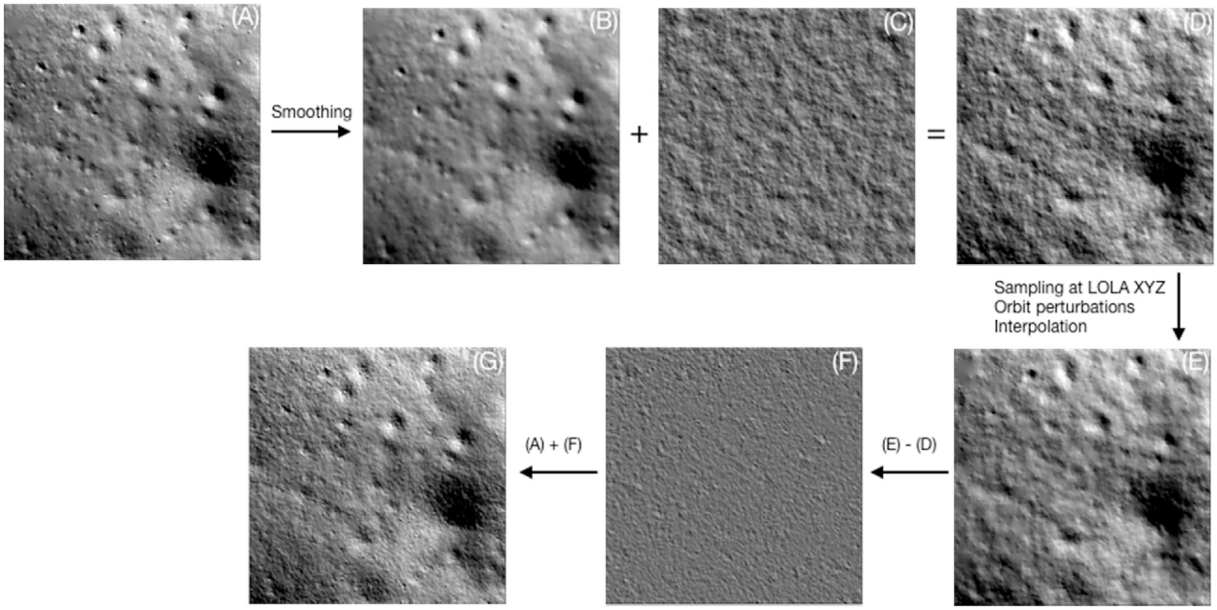

Fig. 11. Flow chart depicting the process to generate a single clone. The region shown is a 2 × 2 km close-up of Site 1 centered at stereographic coordinates (−11, −12) km. The new LDEM (A) is smoothed to make (B), which is then added to a high-pass fractal (C) to make (D). The topography in (D) is then sampled at the LOLA points, which are perturbed by orbital errors, gridded, and interpolated to make (E). The difference (F) between (E) and (D) is a random realization of the errors, which is then added back to the original new LDEM (A) to make a clone (G).

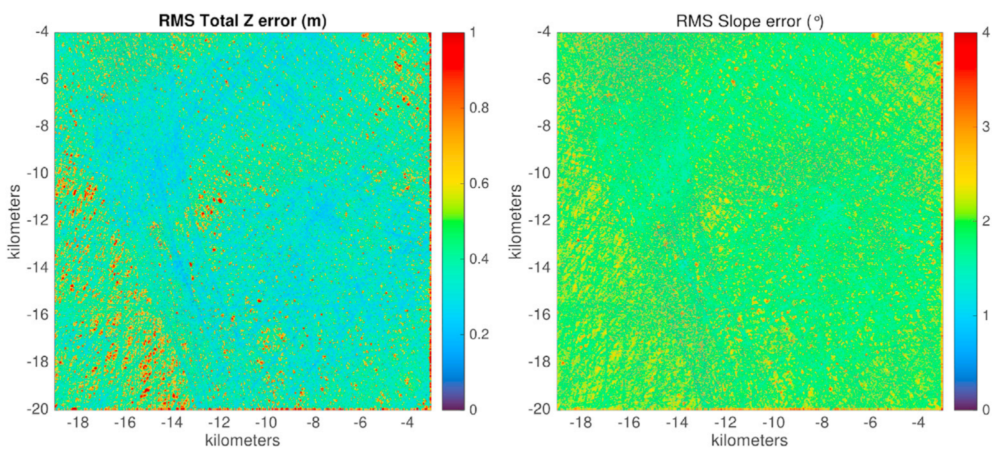

Fig. 12. RMS total Z error (left) and RMS slope error (right) for all 100 clones. The median RMS total Z error is 0.37 m and the MADb is 0.15 m. Approximately 1% of pixels have RMS Z error values > 1 m, ~0.025% have values > 2 m, and the maximum value is 5.65 m. The median RMS slope error is 1.90 deg while the MADb is 0.37 deg. Approximately 1% of pixels have slope error >4°, ~0.01% have values > 9°, and the maximum value is 21°.

points according to two criteria: (1) high slope and (2) runs of large residuals.

Isolated outliers can be identified based on their abnormally high slope relative to the typical slope and roughness of the local terrain. To that end, we computed median-filtered maps of local slope and roughness (MAD_b of slope) binned at 125 m/pix and then we interpolated those maps at each point's location. We then created a test statistic, Δ, which measured the statistical significance of each point's individual slope deviation from the local slope normalized by the local roughness. Points in the tails of the distribution of Δ outside a critical value, $|\Delta_{cr}|$, are considered bad and removed if they have a two-sided probability of $\Delta \leq 0.1\%$ (*i.e.*, $pval_1 \leq 0.001$). We find that, for Site 1, $|\Delta_{cr}| \sim 6$ which yields ~1300 bad points. We did not find visual counterparts to the vast majority of these bad points in NAC images which suggests that the majority are truly spurious noise returns.

This slope test was effective at removing isolated outliers, but we found an additional step was needed to remove a few runs of consecutive bad points. These runs tend to occur in sparser-than-average tracks when the orbit is aligned with the terminator, suggesting some residual pointing fluctuations related to the thermal blanket anomaly (Smith et al., 2017). We constructed the probability distribution of run length for points with absolute residuals >3 times the MAD_b of all 5th iteration residuals. Bad runs were defined as those with a two-sided probability ≤ 0.1%, *i.e.*, $pval_2 \leq 0.001$. Such runs with lengths in the tails of the distribution were removed. For Site 1, this gives a critical run length of 9 points yielding 20 bad runs with ~300 individual points total. Thus, ~1600 points were rejected from Site 1 (Fig. 6 shows some examples) based on $pval_1$ and $pval_2$, or ~0.13% of the ~1 million total.

3.3. Comparison to previous DEMs

Fig. 7 and Fig. S1 - S3 show 4 × 4 km close-ups of each site comparing the old 5 m/pix LDEM (left column) and the new LDEM that we derive (right column). The hillshade (top row) and slope map (bottom row)

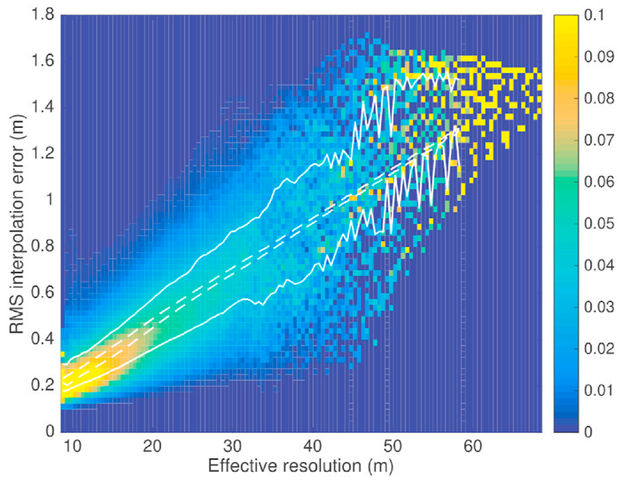

Fig. 13. Correlation between RMS interpolation error and effective resolution (a proxy for gap size). Each column of the 2-D histogram is normalized to the number of points in that column. The best-fit model is a linear combination of effective resolution and surface slope. Solid and dashed lines show the central 50% of the data and model, respectively.

Table 1
Coefficients of regression model ε = a × R + b × S + c, where ε is interpolation error (m) or slope error (°), R is effective resolution (m), and S is slope (°). Formal uncertainties are given for each coefficient.

		Site 1	Site 4	Site 7	Site 11
Interpolation error (m)	*a*	0.0210 ± 0.0002	0.0137 ± 0.0003	0.0209 ± 0.0002	0.0186 ± 0.0002
	b	0.0051 ± 0.0001	0.0074 ± 0.0001	0.0042 ± 0.0001	0.0054 ± 0.0001
	c	−0.022 ± 0.004	−0.006 ± 0.004	−0.0400 ± 0.003	−0.036 ± 0.004
Slope error (°)	*a*	0.0260 ± 0.0002	0.0080 ± 0.0003	0.0235 ± 0.0001	0.0174 ± 0.0002
	b	0.0091 ± 0.0001	0.0149 ± 0.0002	0.0070 ± 0.0001	0.0081 ± 0.0002
	c	1.387 ± 0.004	1.194 ± 0.005	1.373 ± 0.003	1.308 ± 0.004

show how the track adjustment and cleaning process (Section 3.2) have removed the vast majority of streaky artifacts and bad points. The largest improvements occur over regions of high slope since a constant horizontal geolocation error can translate to a larger vertical error in surface height as slope increases.

A simulated image using the new LDEM (Fig. 8, top-right) is a closer match than the old one (top-left) to a NAC 1 m/pix image (bottom-right). The new LDEM resolves ~100 m-diameter craters more consistently than the old one especially over sloped terrain. Craters below this size are still under-represented in the LDEM due to gaps between tracks (*i.e.*, sampling, or fill factor, depends on resolution; 5 m/pix: 7–10%, 20 m/pix: 69–78%, 40 m/pix: 96–98%). On the other hand, the new LDEM does not have any artifacts in and around shadows that can appear when using a NAC 2 m/pix SPG-based DEM (bottom-left; Gläser et al., 2014; http://wms.lroc.asu.edu/lroc/view_rdr/NAC_DTM_ESALL_CR1, last accessed March 2020). Numerous craters visible in the NAC 1 m/pix image in Fig. 8 are below the resolution limit of all three simulated images.

4. LDEM uncertainties

The error-covariance matrix is estimated for each track to obtain the formal track offset uncertainties and their correlations. The formal uncertainties, $\sigma_x/\sigma_y/\sigma_z$, provide a reasonable estimate of the standard deviation of track offsets, $s_x/s_y/s_z$, and therefore, the true uncertainties (Fig. 9). After the final iteration, the orbital errors have been reduced to ~10–20 cm horizontally and ~2–4 cm vertically for most tracks. These formal uncertainties are necessary to specify the covariance between the X/Y/Z components when modeling the orbital errors as discussed below.

Detailed landing site studies may require knowledge of the spatially varying LDEM height errors. However, computation of the full error-covariance matrix of the LDEM (a ~10 million by 10 million non-sparse matrix) would be prohibitive. Instead, we apply a Monte Carlo approach similar to that used in the analysis of the GRAIL lunar gravity field (Lemoine et al., 2014). Instead of calculating the full error-covariance matrix, we create an ensemble of random realizations of the errors of the topography model (*i.e.*, LDEM). These errors can be considered to have a data component, due to orbital errors and interpolation, and a geologic component, due to natural terrain variations.

A variety of studies have found that lunar surface topography exhibits fractal behavior on baselines from ~0.1 mm to 10 cm (Helfenstein and

Table 2
Summary of illumination conditions for all 100 clones at Site 1 RoIs between Jan. 1, 2024 and Jan. 1, 2026 at Δz = 1 m and 5 m above the surface. "Avg ill-1" is the 1st percentile of average illumination in %, "LCIP-1" is the 1st percentile of LCIP in days, and "LCSP-99" is the 99th percentile of LCSP in days (see also Figs. 16–18). Three different cases are listed: (A) percentiles are computed after averaging the RoI for each clone, (B) percentiles are computed separately for each pixel and then averaged over the RoI, and (C) same as (A) but considering only the most illuminated pixel at each hourly time step.

RoI			1	2	3	4	5	6	7
X (km)			−11.5825	−11.4875	−11.3525	−11.2875	−11.1025	−10.8025	−10.2275
Y (km)			−12.4625	−12.5575	−12.5025	−12.1675	−11.9425	−11.7375	−11.5525
Area (m^2)			8625	7550	3825	13300	10075	10000	7075
Δz = 1 m	**Avg Ill-1**	A	68.03	70.32	67.51	69.61	70.38	71.15	67.36
		B	49.30	55.57	57.60	52.19	56.25	56.56	53.72
		C	85.84	85.75	77.31	86.81	84.47	86.74	83.44
	LCIP-1	A	63.35	113.80	117.86	136.49	142.17	81.01	100.23
		B	25.55	53.68	63.21	56.64	66.19	44.86	67.51
		C	205.38	205.08	176.80	232.50	193.40	205.80	117.71
	LCSP-99	A	16.55	17.84	22.23	13.27	15.24	12.74	14.54
		B	28.56	28.69	28.10	26.92	28.03	19.79	28.25
		C	10.46	10.71	15.79	4.58	4.96	4.71	5.04
Δz = 5 m	**Avg Ill-1**	A	89.26	88.51	84.53	88.12	85.71	87.35	82.79
		B	88.21	87.82	83.64	87.43	84.94	86.97	82.47
		C	91.83	91.24	89.78	91.11	88.38	89.05	84.98
	LCIP-1	A	215.79	216.28	216.89	231.20	218.98	220.98	119.07
		B	210.59	211.88	211.20	230.20	215.70	220.80	118.37
		C	232.50	233.00	233.30	233.40	221.10	221.90	174.92
	LCSP-99	A	5.29	7.31	8.41	4.00	4.52	4.16	5.42
		B	6.14	7.95	9.56	4.30	4.90	4.41	5.52
		C	3.67	5.29	5.54	3.71	3.79	3.12	4.58

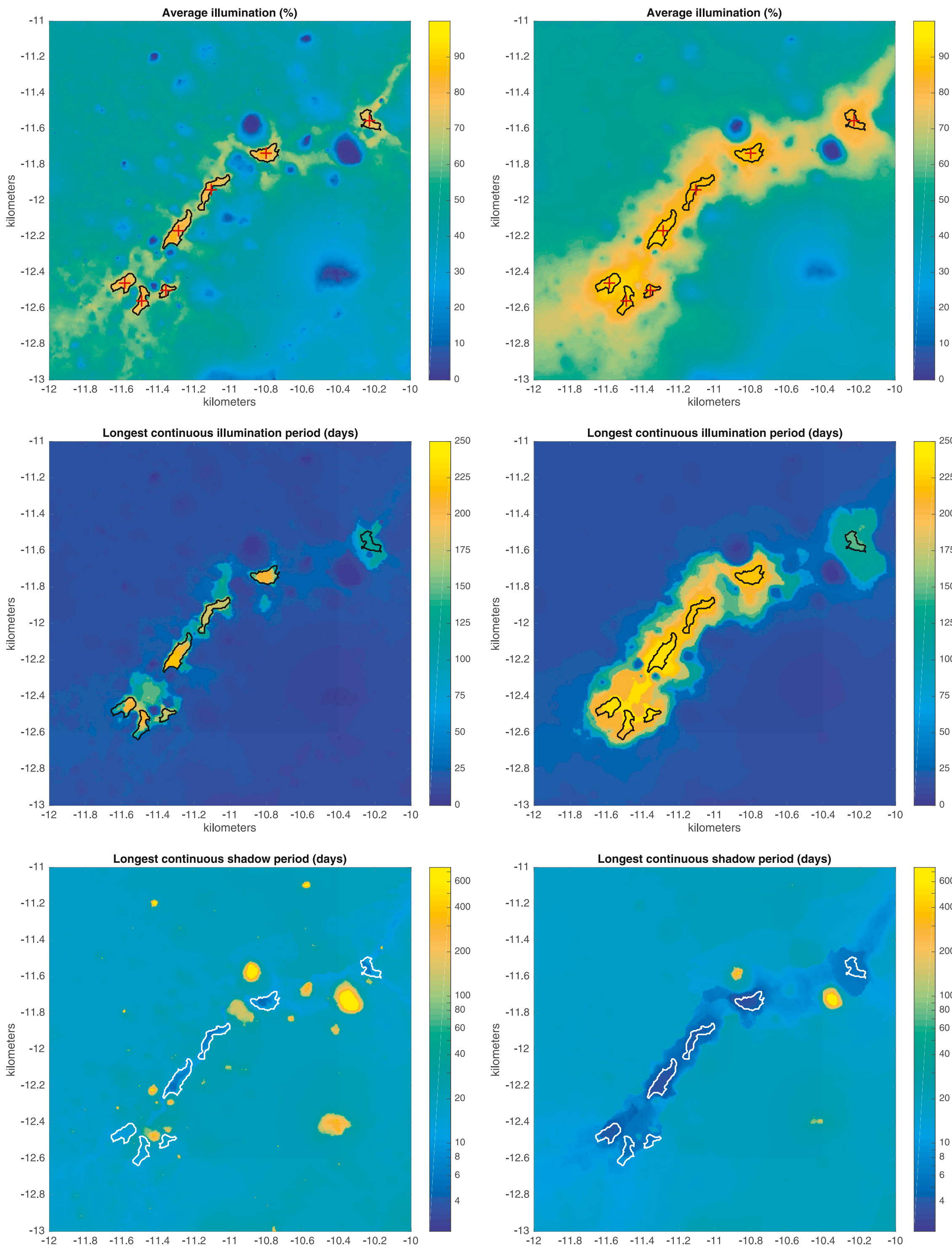

Fig. 14. Illumination conditions at Site 1 between Jan. 1, 2024 and Jan. 1, 2026 at $\Delta z = 1$ m (left column) and 5 m (right column) above the surface. Average illumination (top row) is the average visible fraction of the Sun's disk over the 2 years sampled at 1 h intervals. LCIP (middle row) is the longest uninterrupted period when any fraction of the Sun is visible. LCSP (bottom row) is the longest uninterrupted period when no part of the Sun is visible. The + symbols mark the RoI centroids and the black and white lines denote their boundaries defined as regions with average illumination over 70% between Jan. 1, 2024 and Jan. 1, 2026 and with area over 2500 m^2.

Shepard 1999), and ~20 m to ~1 km (Rosenburg et al., 2011; Kreslavsky et al., 2013; Lemelin et al., 2020). On these scales, the topographic power spectrum follows a power-law with exponent approximately equal to the theoretical expectation of 2+2H for a self-affine randomly rough surface with Hurst exponent H = 1. The power spectra for all 4 sites studied here also behave like an H ≈ 1 power-law (Fig. 10). Excess power on baselines ≳ 10% of the maximum is a bias introduced by undersampling the surface (*i.e.*, long wavelength topography on scales larger than the 16 × 16 km window; Shepard et al., 2001). We can take advantage of the self-similarity of lunar topography to generate simulated terrains with

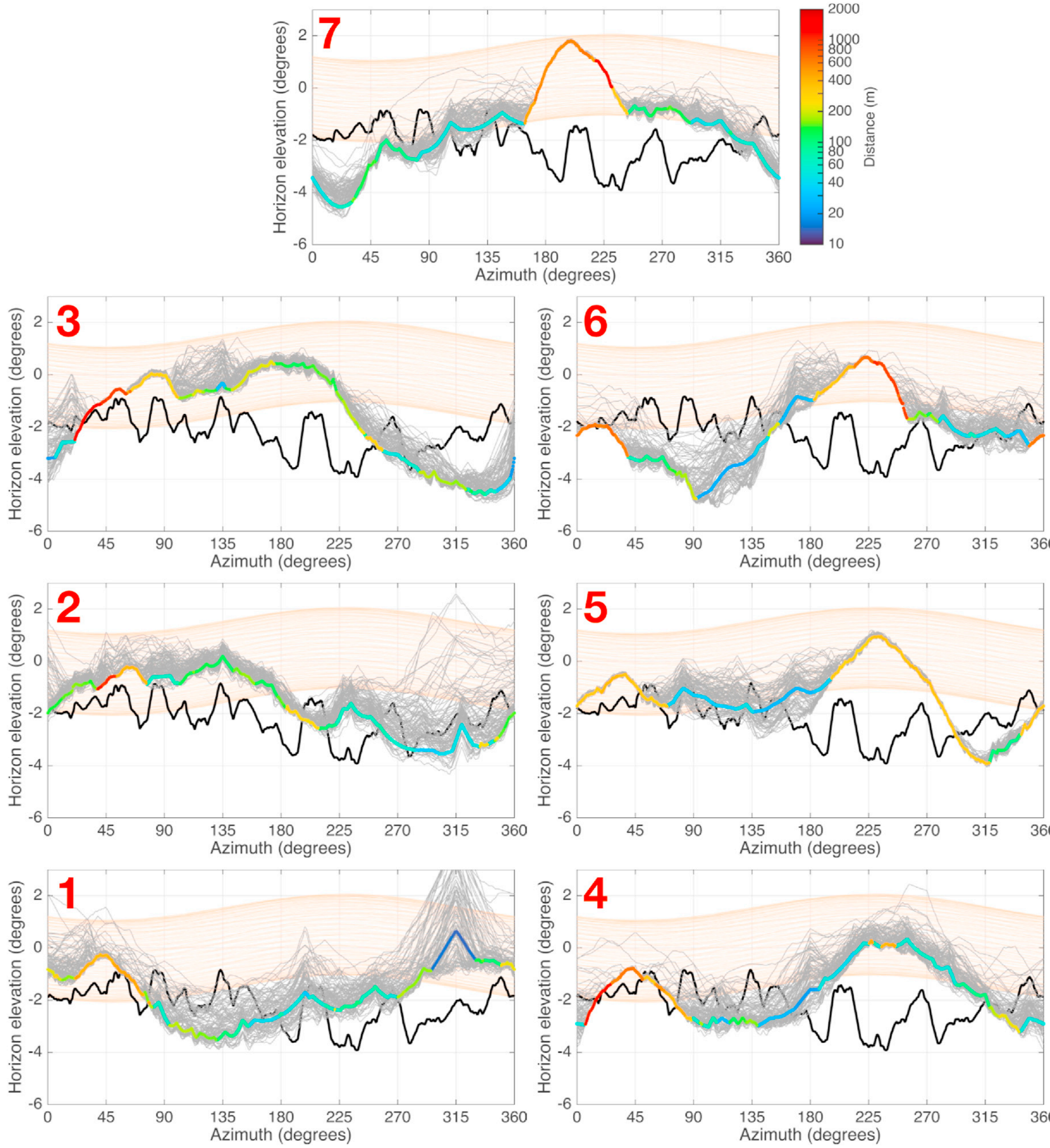

Fig. 15. Horizon maps at the centroids of the RoIs at Site 1 (+symbols in Fig. 14). Each panel compares the horizon viewed from $\Delta z = 1$ m above the surface due to near-field topography in the new LDEM (line colored by distance) and in all 100 clones (gray lines), and the horizon due to far-field topography (black line). The Sun's altitude over 18.6 years starting on Jan. 01, 2024 is shown with orange curves in the background. (For interpretation of the references to color in this figure legend, the reader is referred to the Web version of this article.)

approximately the same statistical properties as the real terrain.

We begin by making a smoothed version of the LDEM (Fig. 11) by removing every LOLA point and its surrounding 3 × 3 pixel neighborhood, and then interpolating to fill the resulting gaps. In the end, this is similar to smoothing with a Gaussian with $\sigma \sim 15$ m, yielding a smoothed version of the actual LDEM with topographic features larger than ~200 m unchanged. This smoothed LDEM is then merged with a high-pass artificial random fractal terrain ($H = 1$) at baselines $\lesssim 200$ m. This particular cut-off baseline was chosen because it was the scale at which a pure fractal terrain lost ~10% of its power after surface interpolation between the filled pixels of the LDEM. This initial simulated terrain is sampled at the LOLA point locations, which are randomly perturbed by the track geolocation errors, $\sigma_x/\sigma_y/\sigma_z$, (according to each track's error-covariance matrix) and 10 cm range (Z) precision, and then surface-interpolated with the same method as for the real data. The difference between this "observationally-filtered" map and the initial simulated map then gives the Z error map for this particular realization. Finally, this Z error map is added back to the LDEM to form a "clone," since the LDEM is our best estimate of the true topography. In total, 100 such clones are generated for each site. These form a statistical ensemble with approximately the same error properties as the data. The clones allow us to explore the effects of orbital error and interpolation uncertainties on surface height and illumination conditions without having to compute the full error-covariance matrix of the entire LDEM.

The uncertainties in surface height shown in Fig. 12 (left panel) are expressed as RMS total height error over all 100 clones for each pixel, or, in other words, the RMS of all 100 versions of panel (F) in Fig. 11. More technically, this map shows what we anticipate the diagonal elements of

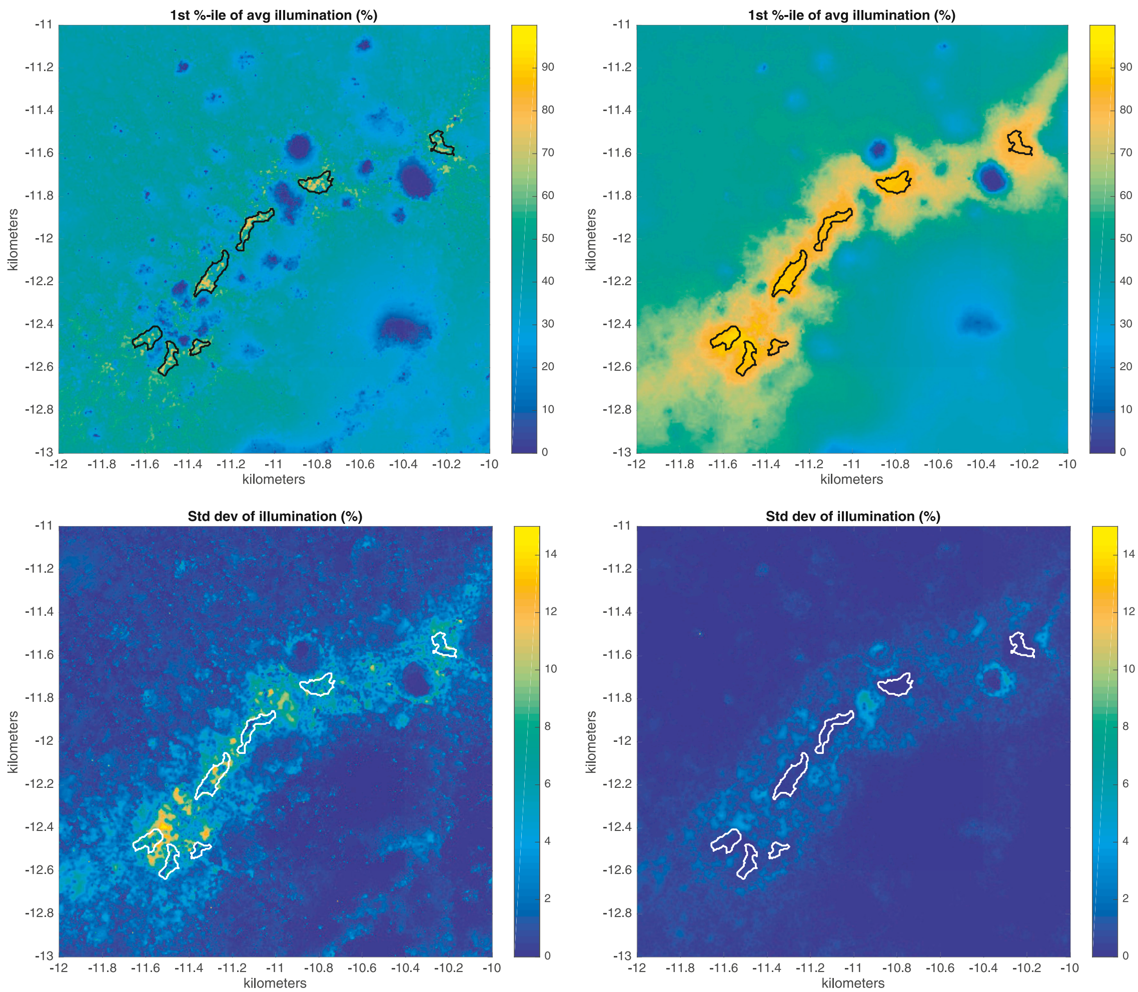

Fig. 16. Uncertainties in average illumination at Site 1 between Jan. 1, 2024 and Jan. 1, 2026 at $\Delta z = 1$ m (left column) and 5 m (right column) above the surface. The 1st percentile (top row) and standard deviation (bottom row) are computed for each pixel independently over all 100 clones. Black and white lines show the boundaries of the RoIs.

the square-root of the full inverse error-covariance matrix would be. The left panel of Fig. 12 could potentially be used as a weight map for the LDEM when constraining higher-resolution DEMs from SPG or SfS. The same map for the other sites is presented in Fig. S4. This map includes interpolation, orbital, range, and sampling errors. Interpolation error dominates in empty pixels, and since ~90% of the pixels are empty, the map is dominated as a whole by interpolation error. In a separate experiment to estimate the effect of interpolation method, we built the clones' true topography with a tension parameter T = 0, while still estimating them with T = 0.75. This resulted in a net increase to the height and slope uncertainties of all pixels (Fig. 12) by a median factor of ~1.1 with a MAD_b of 0.2. We, therefore, take 30% as the uncertainty due to interpolation method.

Because the orbital errors are so small, the LOLA points tend to stay in the same pixels for all clones, and the dominant source of Z error in filled pixels is due to the sampling of LOLA points within the pixels. Thus, the upper envelope of Z errors of filled pixels for any single clone is limited by the pixel size and correlates with slope roughly as ~2.5 sqrt (2) tan (slope). The median RMS Z error is 0.37 m while the MAD_b of the RMS Z error is 0.15 m. Approximately 1% of pixels have RMS Z error values > 1 m, ~0.025% have values > 2 m, and the maximum value over the whole map (>10 million pixels) is 5.65 m. Approximately 2% of *filled* pixels have RMS Z error values > 1 m, ~0.01% have values > 2 m, and the maximum value over all filled pixels is 3.31 m.

Visual inspection of the surface height interpolation error map reveals a correlation with gap size and surface slope, *i.e.*, larger interpolation errors tend to occur over larger gaps and larger slopes. This makes sense intuitively and is borne out by a quantitative comparison in Fig. 13. Regressing the interpolation error simultaneously on effective resolution (a proxy for gap size computed as the inverse square-root of the LOLA point areal density) and surface slope gives coefficients of $a = 0.0210 \pm 0.0002$ and $b = 0.0051 \pm 0.0001$, respectively, with a zero-point of $c = -0.0218 \pm 0.0038$. Apparently, most of the correlation is due to effective resolution (gap size) rather than slope. The scatter scales proportionally with the effective resolution, presumably because larger gaps can accommodate larger height variations. Nevertheless, the model fits the central 50% of the data to within ~30%, and, thus, can provide a useful quick estimate of interpolation error in the new 5 m/pix LDEMs, since effective resolution and slope can be easily calculated. Table 1 lists the fit coefficients for all sites. The slope coefficient for Site 4 is greater than the others because Shackleton's steep wall (~36° slope) covers a large portion of the area.

We also examine slope error since that can affect traverse planning. Traverse studies could use the right panel of Fig. 12 as an uncertainty map for the LDEM slopes. The median RMS slope error is 1.90° while the MAD_b is 0.37°. Approximately 1% of pixels have slope error >4°, ~0.01% have values > 9°, and the maximum value over the whole map is 21°. RMS slope errors >4° tend to occur on slopes $\gtrsim$ 25°. For slopes relevant to most rovers ($\lesssim$ 20°), the central 50% of RMS slope errors does not depend notably on slope, but shows a weak correlation with effective

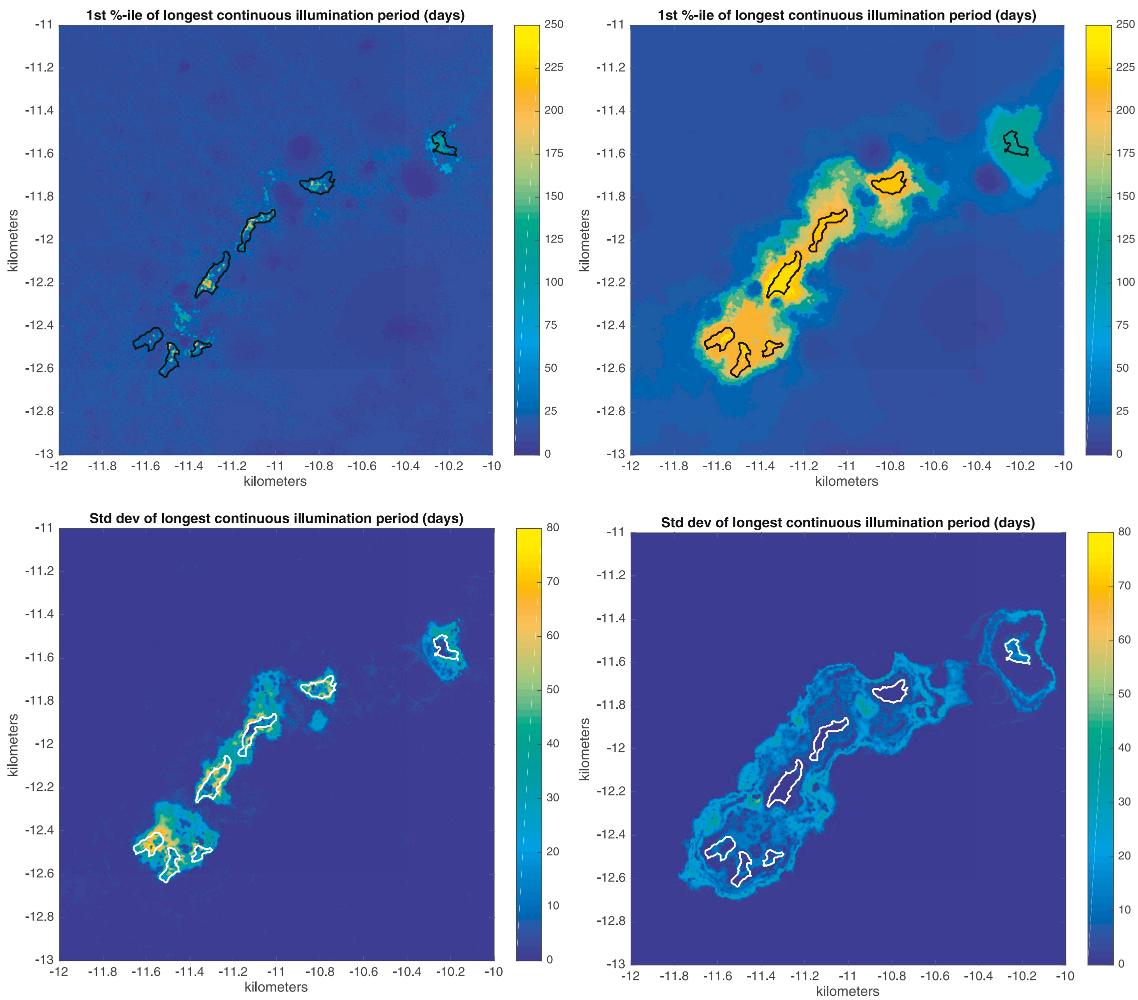

Fig. 17. – Same as Fig. 16, but for LCIP.

resolution. Table 1 lists the simultaneous regression coefficients for slope error with effective resolution and slope.

Several caveats should be considered when interpreting the LDEM uncertainties. First, ~90% of 5 m LDEM pixels in these study areas are empty, so we have used interpolation to fill them in. We have used the self-similarity of lunar topography to simulate what the surface might be like in an average statistical sense. Individual features such as craters and boulders will cause deviations at any given location. Our goal here is to present the new methods and products based on LOLA data that can be used in more complete landing site analyses that would involve detailed assessment of multiple datasets to fill in the gaps at higher resolution. It is possible that deviations from self-affinity become significant at smaller baselines due to pebbles, rocks, and boulders. Currently, our uncertainty analysis does not account for such effects. Diviner thermal measurements at low latitudes indicate a rock abundance of ~0.2–0.5% for typical highlands terrain (Bandfield et al., 2011). Formally, the Diviner rock abundance (DRA) is defined as the fractional areal coverage of rocks > 1 m in diameter. These measurements have been directly validated to within a factor of ~2 with visual boulder counts in NAC images at several young craters (Watkins et al., 2019). De Rosa et al. (2012) performed visual boulder counts at 4 potential south pole landing sites and found a fractional areal coverage one order of magnitude less than the typical DRA value for highlands terrain. Ideally, we would have a full model for the rock size, shape, and spatial distribution and how those within a LOLA spot affect its height measurement. In the absence of that, we can make a broad estimate from earlier work on the LOLA pulse width measurements, which found that the RMS height variation averaged over a single 5 m spot is generally ~0.4–0.6 m over highlands terrain (Neumann et al., 2015).

5. Illumination conditions

For the calculation of illumination conditions (Fig. 14), we use the horizon method outlined in Mazarico et al. (2011) in which the horizon elevation viewed from every pixel is computed along 720 sight lines spaced 0.5° apart in azimuth. We take a nested-grid approach (Mazarico et al., 2018b) in which the new 5 m/pix LDEM is used for distances <5 km, the 80 m/pix original LDEM for distances 5–100 km, and the 240 m/pix original LDEM for larger distances. This approach is much more computationally efficient than using a single resolution. The computations are performed in Cartesian coordinates at 1-h intervals. The Sun is treated as a 2-dimensional extended source with limb darkening at 550 nm, similar to the effective limb darkening when weighting the whole spectrum. The visible fraction of the Sun's disk (*i.e.*, illumination) is approximated by horizontally dividing the disk at the horizon's elevation measured at the disk center's azimuth.

Conceptually, it is helpful to think of the horizon as composed of a near-field component roughly 100 m away (though sometimes as low as 10s of m, or as high as ~1 km) and a far-field component roughly 50–200 km away. The clones allow us to estimate the height error and, by extension, the horizon and illumination error. Fig. 15 illustrates how height error translates to a near-field horizon elevation error. It displays the near-field horizon viewed from $\Delta z = 1$ m above the surface at 7 locations (+symbols in Fig. 14) in the LDEM and the 100 clones. The far-

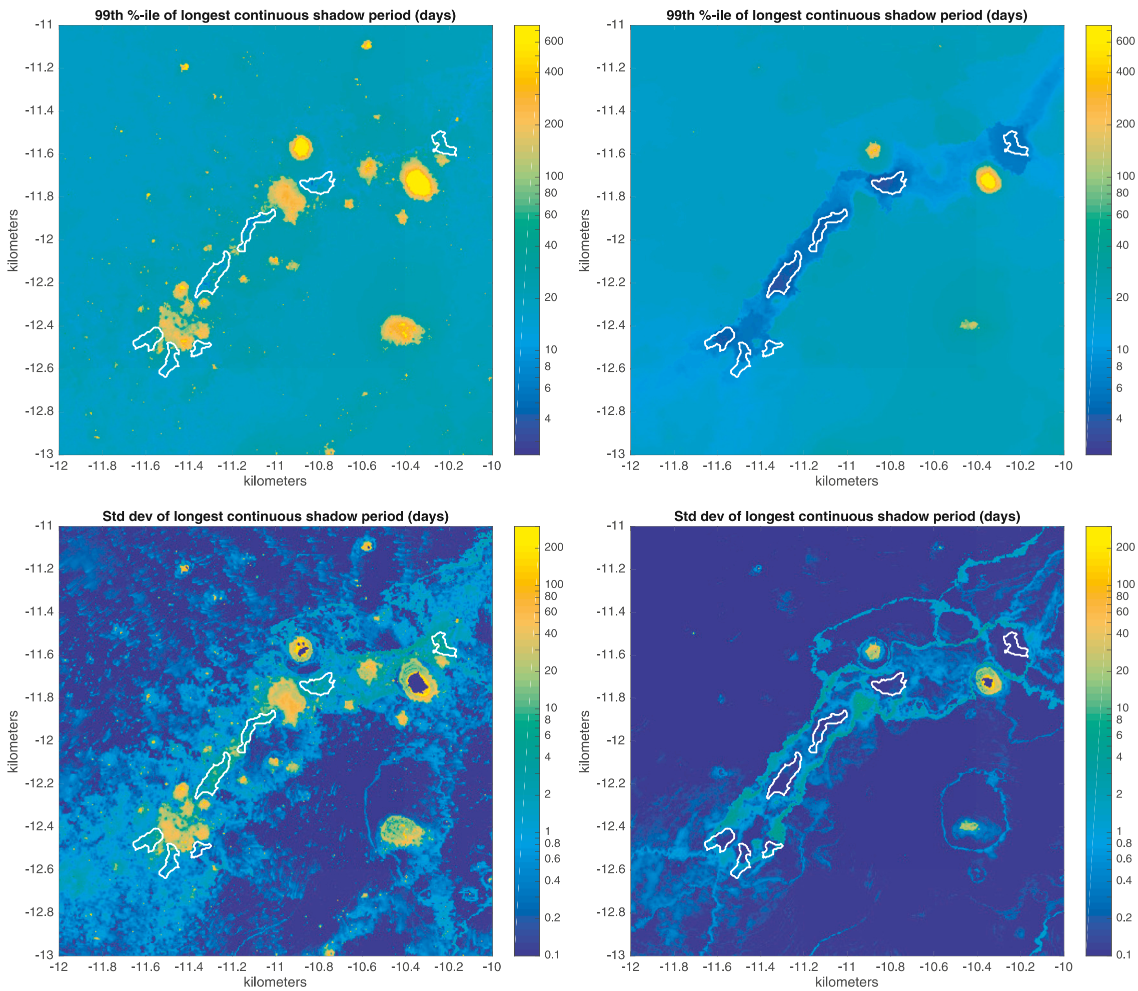

Fig. 18. Same as Fig. 16, but for 99th percentile and standard deviation of LCSP.

field horizon changes negligibly between the different locations. In practice, the horizon computation is not restricted to just two horizon lines, near and far, although conceptually it can be helpful to think of it in those terms. We also note that the un-adjusted orbital errors in the lower-resolution far-field LDEMs do not significantly impact the results presented here because the far-field horizon is ~3 orders of magnitude farther away than the near-field, and those LDEMs' larger pixels average over many more LOLA spots.

Fig. 14 shows the illumination conditions in the new LDEM at Site 1 between Jan. 1, 2024 and Jan. 1, 2026 at two different heights above the surface, $\Delta z = 1$ m and 5 m. The top row is the average illumination defined as the average visible fraction of the Sun's disk over the 2 years. It does not directly translate to how much of the Sun is visible at any given time. For example, a pixel with average illumination of 50% could see half the Sun for the entire time period, or the whole Sun for half the time period. The bottom row shows the longest continuous illumination period (LCIP) defined as the longest uninterrupted period when any fraction of the Sun is visible. Again, this does not say anything about when that uninterrupted period occurs. Similarly, the bottom row shows the longest continuous shadow period (LCSP) defined as the longest uninterrupted period when none of the Sun is visible.

At each site, we identified regions-of-interest (RoIs) of connected pixels (corners or sides touching) with average illumination > 70% at $\Delta z = 1$ m and with total area >2500 m^2 (Fig. 3). Site 1 had the most RoIs with the most area satisfying these criteria. At 5 m above the surface of Site 1, the RoIs merge and nearly the entire connecting ridge has an average illumination >70% (Fig. 14). As noted in previous work, this highlights the dramatic difference in illumination that a few meters of height can make and, thus, the importance of raising a landed asset's solar panels as high as possible (Mazarico et al., 2011; De Rosa et al., 2012; Gläser et al., 2018).

To examine the impact of the height errors on the illumination conditions, we perform the same computations on each of the 100 clones independently and examine certain relevant statistics for the whole ensemble (Table 2). This is a computationally expensive process, and, to our knowledge, has not been done extensively before. Maps of the 1st or 99th percentile (minimum and maximum) and standard deviation (Figs. 16, 17 and 18,) show that the RoIs have varying amounts of uncertainty, but that they tend to have relatively low uncertainties compared to their immediate surroundings.

The RoI centroids (+symbols in Fig. 14) are of interest because they may be targets for a lander. However, the probability of actually landing on those exact pixels is small given the NASA Artemis Human Landing System requirement of a 100 m-radius landing ellipse[2]. Hence, we consider all the pixels within each RoI when computing their statistics in Table 2. Similarly, Fig. 19 shows box plots of the illumination conditions for all pixels within each RoI at $\Delta z = 1$ m. Table 2 and Fig. 19 can be used to rank the RoIs when choosing a landing site. The box plots show the distributions of the 100 clones when the pixels within each RoI for each clone are averaged together. Hence, the min/max values of the box plots

[2] Human Landing System (HLS) Requirements Document, HLS-RQMT-001, https://beta.sam.gov/opp/d5460a204ab23cc0035c088dcc580d17/view.

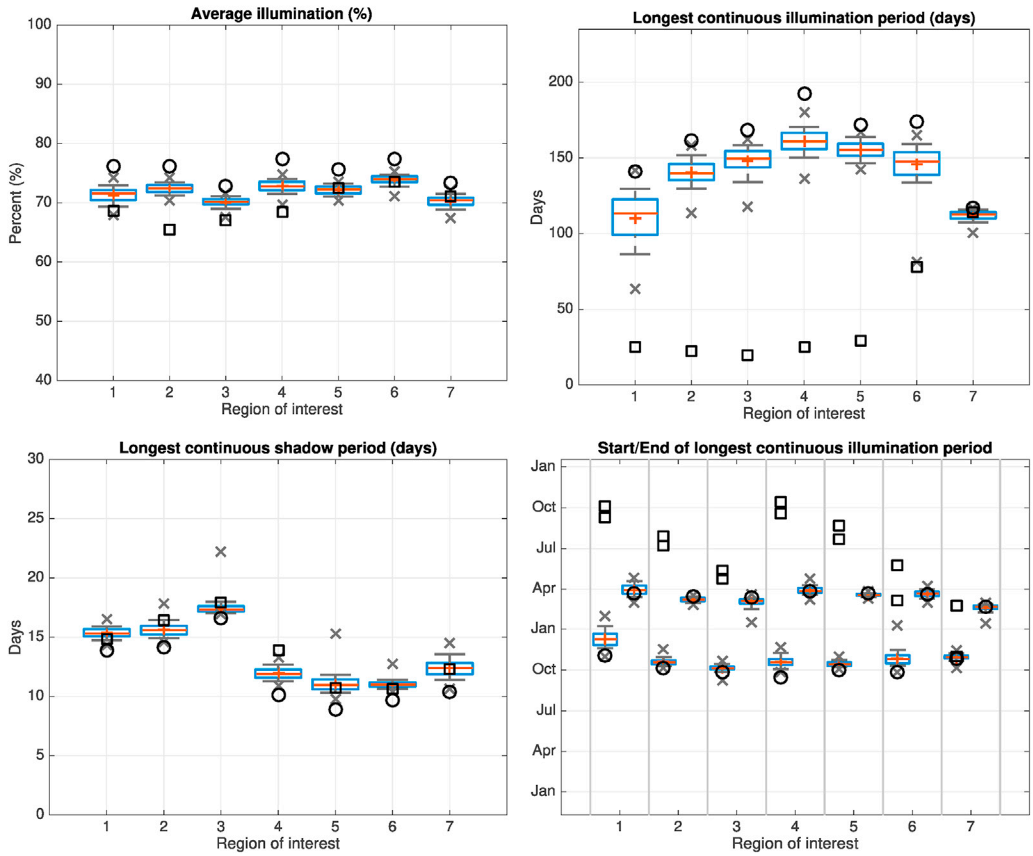

Fig. 19. Box plots of illumination conditions at Site 1 between Jan. 1, 2024 and Jan. 1, 2026 at Δz = 1 m above the surface averaged over each RoI in the old LDEM (squares), new LDEM (circles) and 100 clones: mean (+), median (−), inter-quartile range (box), 9th/91st percentiles (whiskers), and min/max (x). The width of each distribution reflects the overall uncertainty in illumination conditions at each location.

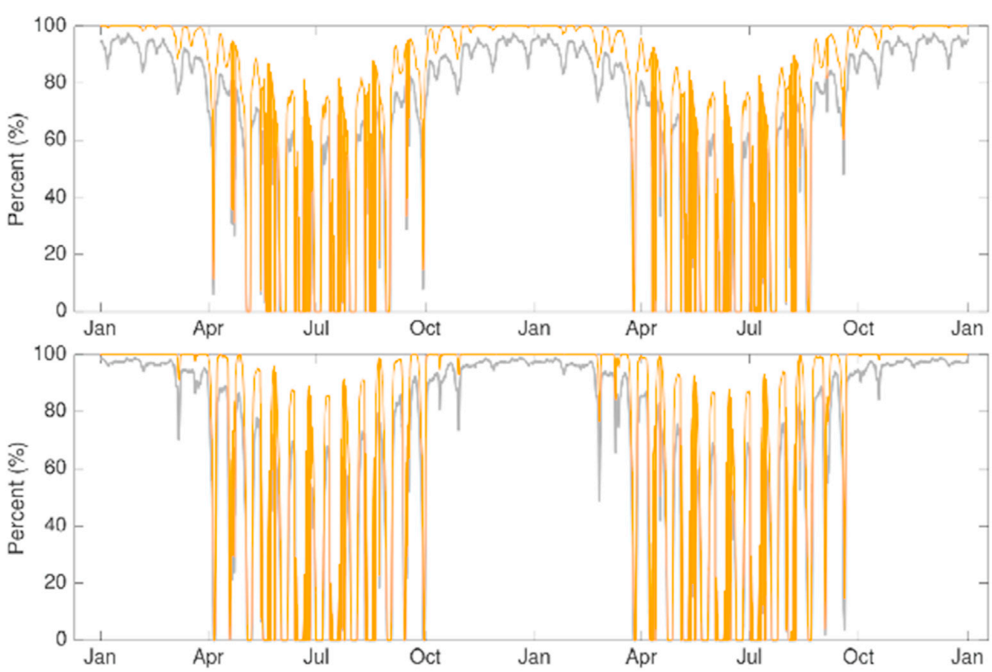

Fig. 20. Variation of illumination between Jan. 1, 2024 and Jan. 1, 2026 for Site 1 averaged over all pixels in RoI 6 (top) and RoI 5 (bottom) at Δz = 1 m above the surface. Gray lines are the minimum of all clones' RoI averages at each time step and orange lines are the LDEM. Some clones have short periods of reduced illumination in southern summer due to height uncertainties in the LDEM. (For interpretation of the references to color in this figure legend, the reader is referred to the Web version of this article.)

(x symbols in Fig. 19) correspond to the 1st/99th percentiles listed in Table 2, A rows. Narrower distributions imply smaller uncertainties in the illumination conditions. At Δz = 1 m, the 1st percentile of average illumination ranges from 67% (RoI 7) to 71% (RoI 6), the 1st percentile of LCIP ranges from 63 days (RoI 1) to 142 days (RoI 5), and the 99th percentile of LCSP ranges from 13 days (RoI 4 and 6) to 22 days (RoI 3). Increasing the height above the surface to Δz = 5 m greatly improves the illumination conditions, so that the 1st percentile of average illumination ranges from 83% (RoI 7) to 89% (RoI 1), the 1st percentile of LCIP ranges from 119 days (RoI 7) to 231 days (RoI 4), and the 99th percentile of LCSP ranges from 4 days (RoI 4–6) to 8 days (RoI 3). The squares in Fig. 19 show that, as expected, the old (non-clone) LDEM has worse illumination conditions than the new one. Notably, the illumination conditions predicted for the new (non-clone) LDEM (open circles in Fig. 19) tend to be better than the mean/median of the clones, which shows that considering errors will usually result in less favorable conditions. This is because the perturbations in the clones are more likely to raise than lower the horizon elevation. All it takes to raise the horizon elevation is one positive height fluctuation with sufficient magnitude along the line-of-sight. In contrast, lowering the horizon requires a less likely set of circumstances, in which the positive fluctuations at multiple distances near the observer and near the original horizon are small.

Averages of all individual pixels' 1st and 99th percentiles (Table 2, B rows) offer a pessimistic scenario since the chances of all pixels within a RoI having the same percentile error is likely smaller than a single pixel even considering their correlations. As an optimistic scenario, Table 2, C rows consider only the most highly illuminated pixel within a RoI at each hourly time step of the simulation, so that LCIP/LCSP includes time steps when any/no pixel in the RoI sees any part of the Sun. In this case, at $\Delta z = 1$ m, the 1st percentile of average illumination ranges from 77% (RoI 3) to 87% (RoI 4 and 6), the 1st percentile of LCIP ranges from 118 days (RoI 7) to 232 days (RoI 4), and the 99th percentile of LCSP ranges from 4 days (RoI 4) to 16 days (RoI 3). Therefore, roving capability within each RoI dramatically improves the illumination conditions and decreases the impact of height uncertainties at $\Delta z = 1$ m. On the other hand, adding mobility to a lander with 5-m-high solar panels does not make as big a difference, increasing the 1st percentile of average illumination by ~2–5% and decreasing LCSP's 99th percentile by ~1–3 days, from ~4–8 down to ~3–6 days (Table 2, $\Delta z = 5$ m, A vs. C rows).

The time variation of illumination (Fig. 20) shows similar seasonal and monthly patterns among the RoIs with higher illumination during southern lunar summer. Some of the clones have short periods of reduced illumination in southern summer due to height uncertainties in the LDEM. We note that the detailed illumination conditions and time variation will exhibit additional periodic variations on longer timescales than simulated here, such as the 18.6 yr precession period.

Maps and box plots of illumination conditions at the other sites are presented in Fig. S5 – S19. The LDEM height and slope uncertainties within the RoIs are similar across all the sites with a median RMS Z error ~0.30–0.50 m and a median RMS slope error ~1.5–2.5°. Despite the similar height uncertainties, differences in the near-field topography can lead to different illumination uncertainties. The clone illumination simulations for all the sites show that RoIs 4–6 at Site 1 generally have the most favorable illumination conditions at $\Delta z = 1$ m even considering their uncertainties (1st and 99th percentiles). At $\Delta z = 5$ m, the average illumination and LCSP are more similar between the different sites, but Site 1 tends to have significantly longer LCIP, (*i.e.*, LCIP > 200 days for RoIs 1–6 compared to ~150–175 days for the other sites). The LDEM uncertainties have an almost negligible effect on the illumination conditions at $\Delta z = 5$ m at all sites, showing an added benefit of raising solar panels several meters above surface level.

6. Conclusions

We have derived new high-resolution DEMs of four 16 × 16 km regions surrounding high-priority lunar south pole landing sites using exclusively laser altimetry data acquired by LRO-LOLA. By iteratively co-adjusting the LOLA tracks in a self-consistent fashion, we reduced the orbital errors by over a factor of 10 such that the new track geolocation uncertainty is ~10–20 cm horizontally and ~2–4 cm vertically over each region. The new 5 m/pix LDEMs are substantially more realistic than the previous ones with fewer artifacts due to orbital errors and fewer spurious noise points. While the fraction of interpolated 5-m pixels in these polar LDEMs is necessarily large (~90%) due to LOLA's cross-track and inter-spot spacing, these LDEMs have the advantage of having accurate geodetic control and of being unaffected by shadows, and, thus, will be useful constraints on higher-resolution topographic models derived from imagery.

We developed a method to estimate surface height uncertainty in the new LDEMs that accounts for the reduced orbital errors and interpolation errors. This method circumvents the infeasible computation of the full error-covariance matrix of the LDEM. Instead, we use the fractal nature of lunar topography to build a more computationally manageable statistical ensemble of clones with similar error properties as the data. We show how we use this ensemble to study height and slope uncertainty, as well as the uncertainty in illumination conditions. Such an approach can be useful for a range of other studies, not just pure illumination conditions, when examining the feasibility of potential landing sites.

The LDEM height and slope uncertainties within the RoIs are similar across all the sites with a median RMS Z error ~0.30–0.50 m and a median RMS slope error ~1.5–2.5°. Interpolation error depends primarily on gap size, or areal density of the LOLA points, with a secondary dependence on terrain slope that becomes more important over highly sloped terrain. Hence, the interpolation error will be larger at greater distances from the pole for the same pixel scale, because of the lower point density and poorer effective resolution. The illumination conditions within each RoI are impacted by height uncertainties and show more variation that can potentially be used as a guide to rank the different sites and RoIs within a site. Between Jan. 1, 2024 and Jan. 1, 2026, Site 1 has the most area with average illumination >70% at 1 m above the surface and RoIs 4–6 at this site generally have the most favorable illumination conditions even considering their uncertainties. At 5 m above the surface, the effect of LDEM uncertainties on illumination conditions are significantly reduced, and Site 1 has longer continuous illumination periods than the other sites.

CRediT authorship contribution statement

Michael K. Barker: Conceptualization, Methodology, Software, Validation, Formal analysis, Data curation, Visualization, Writing - original draft. **Erwan Mazarico:** Conceptualization, Methodology, Software, Data curation, Visualization, Supervision, Writing - review & editing. **Gregory A. Neumann:** Writing - review & editing. **David E. Smith:** Writing - review & editing. **Maria T. Zuber:** Writing - review & editing. **James W. Head:** Writing - review & editing.

Declaration of competing interest

The authors declare that they have no known competing financial interests or personal relationships that could have appeared to influence the work reported in this paper.

Acknowledgements

We are grateful to the LRO Mission Operations Team for their tireless work in making LRO a successful mission. Resources supporting this work were provided by the NASA High-End Computing (HEC) Program through the NASA Center for Climate Simulation (NCCS) at Goddard Space Flight Center. Support for this research was provided by NASA's Planetary Science Division Research Program.

Appendix A. Supplementary data

Supplementary data to this article can be found online at https://doi.org/10.1016/j.pss.2020.105119.

Data availability

The new DEMs, clones, and uncertainty maps presented in this paper are available publicly at the LOLA PDS Data Node (http://imbrium

.mit.edu/) and at the Planetary Geodynamics Data Archive (https://pgda.gsfc.nasa.gov/).

References

Alexandrov, O., Beyer, R.A., 2018. Multiview shape-from-shading for planetary images. Earth Space Sci. 5, 652–666. https://doi.org/10.1029/2018EA000390.

Arnold, J.R., 1979. Ice in the lunar polar regions. J. Geophys. Res.: Solid Earth 84 (B10), 5659–5668. https://doi.org/10.1029/JB084iB10p05659.

Bandfield, J.L., Ghent, R.R., Vasavada, A.R., Paige, D.A., Lawrence, S.J., Robinson, M.S., 2011. Lunar surface rock abundance and regolith fines temperatures derived from LRO Diviner radiometer data. J. Geophys. Res. 116, E00H02. https://doi.org/10.1029/2011JE003866.

Barker, M.K., Sun, X., Mao, D., Mazarico, E., et al., 2018. In-flight characterization of the Lunar Orbiter Laser Altimeter instrument pointing and far-field pattern. Appl. Optic. 57, 7702–7713. https://doi.org/10.1364/AO.57.007702.

Bryant, S., 2009. Lunar pole illumination and communications maps computed from Goldstone Solar System Radar elevation data. Aero. Conf. IEEE. https://doi.org/10.1109/AERO.2009.4839375.

Bussey, D.B.J., Spudis, P.D., Robinson, M.S., 1999. Illumination conditions at the lunar south Pole. Geophys. Res. Lett. 26, 1187–1190. https://doi.org/10.1029/1999GL900213.

Bussey, D., McGovern, J., Spudis, P., Neish, C., Noda, H., Ishihara, Y., Sørensen, S.-A., 2010. Illumination conditions of the south pole of the Moon derived using Kaguya topography. Icarus 208, 558–564. https://doi.org/10.1016/j.icarus.2010.03.028.

Colaprete, A., Elphic, R.C., Shirley, M., et al., 2020. The volatiles investigating polar exploration rover (VIPER) mission: measurement goals and traverse planning. Lunar Planet. Sci. 51. Abstract 2241.

De Rosa, D., Bussey, B., Cahill, J.T., et al., 2012. Characterization of potential landing sites for the European Space Agency's lunar lander project. Planet. Space Sci. 74, 224–246. https://doi.org/10.1016/j.pss.2012.08.002.

Fincannon, J., 2007. Lunar South Pole Illumination: Review, Reassessment, and Power System Implications. American Institute of Aeronautics and Astronautics, p. 4700. https://doi.org/10.2514/6.2007-4700, 2007.

Fisher, E.A., Lucey, P.G., Lemelin, M., Greenhagen, B.T., Siegler, M.A., Mazarico, E., et al., 2017. Evidence for surface water ice in the lunar polar regions using reflectance measurements from the Lunar Orbiter Laser Altimeter and temperature measurements from the Diviner Lunar Radiometer Experiment. Icarus 292, 74–85. https://doi.org/10.1016/j.icarus.2017.03.023.

Flahaut, J., Carpenter, J., Williams, J.-P., et al., 2020. Regions of interest (ROI) for future exploration missions to the lunar south pole. Planet. Space Sci. 180, 104750. https://doi.org/10.1016/j.pss.2019.104750.

Folkner, W.M., Williams, J.G., Boggs, D.H., 2009. The planetary and lunar ephemeris DE 421. Interplanetary Network Prog. Rep. 42–178, 1–34.

Gläser, P., Scholten, F., De Rosa, D., Figuera, R.M., Oberst, J., Mazarico, E., Neumann, G.A., Robinson, M.S., 2014. Illumination conditions at the lunar south pole using high resolution digital terrain models from LOLA. Icarus 243, 78–90. https://doi.org/10.1016/j.icarus.2014.08.013.

Gläser, P., Oberst, J., Neumann, G.A., Mazarico, E., Speyerer, E.J., Robinson, M.S., 2018. Illumination conditions at the lunar poles: implications for future exploration. Planet. Space Sci. 162, 170–178. https://doi.org/10.1016/j.pss.2017.07.006.

Hayne, Paul O., Hendrix, A., Sefton-Nash, E., Siegler, M.A., Lucey, P.G., Retherford, K.D., et al., 2015. Evidence for exposed water ice in the Moon's south polar regions from Lunar Reconnaissance Orbiter ultraviolet albedo and temperature measurements. Icarus 255, 58–69. https://doi.org/10.1016/j.icarus.2015.03.032.

Heldmann, J.L., Colaprete, A., Elphic, R.C., Bussey, B., McGovern, A., Beyer, R., Lees, D., Deans, M., 2016. Site selection and traverse planning to support a lunar polar rover mission: a case study at Haworth Crater. Acta Astronaut. 127, 308–320. https://doi.org/10.1016/j.actaastro.2016.06.014.

Henriksen, M.R., Manheim, M.R., Burns, K.N., et al., 2017. Extracting accurate and precise topography from LROC narrow angle camera stereo observations. Icarus 283, 122–137. https://doi.org/10.1016/j.icarus.2016.05.012.

Huber, P.J., 1981. Robust Statistics. John Wiley, New York.

Ivanov, M.A., Hiesinger, H., Abdrakhimov, A.M., et al., 2015. Landing site selection for Luna-Glob mission in crater Boguslawsky. Planet. Space Sci. 117, 45–63. https://doi.org/10.1016/j.pss.2015.05.007.

Kreslavsky, M.A., Head, J.W., Neumann, G.A., Rosenburg, M.A., Aharonson, O., Smith, D.E., Zuber, M.T., 2013. Lunar topographic roughness maps from Lunar Orbiter Laser Altimeter (LOLA) data: scale dependence and correlation with geologic features and units. Icarus 226, 52–66. https://doi.org/10.1016/j.icarus.2013.04.027.

Lemelin, M., Daly, M.G., Deliege, A., 2020. Analysis of the Topographic Roughness of the Moon Using the Wavelet Leaders Method and the Lunar Digital Elevation Model From the Lunar Orbiter Laser Altimeter and SELENE Terrain Camera. J. Geophys. Res.: Plan. 125 (1), e06105. https://doi.org/10.1029/2019JE006105.

Lemoine, F.G., Goossens, S., Sabaka, T.J., et al., 2014. GRGM900C : a degree 900 lunar gravity model from GRAIL primary and extended mission data. Geophys. Res. Lett. 41, 3382–3389. https://doi.org/10.1002/2014GL060027.

Leys, C., Ley, C., Klein, O., et al., 2013. Detecting outliers: do not use standard deviation around the mean, use absolute deviation around the median. J. Exp. Soc. Psychol. 49, 764–766. https://doi.org/10.1016/j.jesp.2013.03.013.

Li, S., Lucey, P.G., Milliken, R.E., Hayne, P.O., Fisher, E., Williams, J.-P., et al., 2018. Direct evidence of surface exposed water ice in the lunar polar regions. Proc. Natl. Acad. Sci. Unit. States Am. 115, 8907–8912. https://doi.org/10.1073/pnas.1802345115.

Mazarico, E., Neumann, G.A., Smith, D.E., Zuber, M.T., Torrence, M.H., 2011. Illumination conditions of the lunar polar regions using LOLA topography. Icarus 211 (2), 1066–1081. https://doi.org/10.1016/j.icarus.2010.10.030.

Mazarico, E., Neumann, G.A., Barker, M.K., Goossens, S., Smith, D.E., Zuber, M.T., 2018a. Orbit determination of the lunar reconnaissance orbiter: status after seven years. Planet. Space Sci. 162, 2–19. https://doi.org/10.1016/j.pss.2017.10.004.

Mazarico, E., Barker, M.K., Nicholas, J.B., 2018b. Advanced illumination modeling for data analysis and calibration. Application to the Moon. Adv. Space Res. 62, 3214–3228. https://doi.org/10.1016/j.asr.2018.08.022.

Neumann, G.A., Glaeser, P.A., Hiesinger, H., Zuber, M.T., Smith, D.E., 2015. Copernican-age craters and LOLA decameter-scale roughness. Lunar Planet. Sci. 46. Abstract 2218.

Noda, H., Araki, H., Goossens, S., Ishihara, Y., Matsumato, K., Tazawa, S., Kawano, N., Sasaki, S., 2008. Illumination conditions at the lunar polar regions by kaguya (selene) laser altimeter. Geophys. Res. Lett. 35, L24203. https://doi.org/10.1029/2008GL035692.

Ohtake, M., Karouji, Y., Inoue, H., Shiraishi, H., Hoshino, T., et al., 2020. Objective and configuration of a planned lunar polar exploration. Lunar Planet. Sci. 51. Abstract 1830.

Polat, E., 2020. The effects of different weight functions on partial robust M-regression performance: a simulation study. Commun. Stat. Simulat. Comput. 49, 1089–1104. https://doi.org/10.1080/03610918.2019.1586926.

Rosenburg, M.A., Aharonson, O., Head, J.W., Kreslavsky, M.A., Mazarico, E., Neumann, G.A., et al., 2011. Global surface slopes and roughness of the Moon from the lunar orbiter laser altimeter. J. Geophys. Res.: Plan 116 (E2). https://doi.org/10.1029/2010JE003716.

Shepard, M.K., Campbell, B.A., Bulmer, M.H., et al., 2001. The roughness of natural terrain: a planetary and remote sensing perspective. J. Geophys. Res. 106 (E12), 777–795. https://doi.org/10.1029/2000JE001429.

Smith, D.E., Zuber, M.T., Neumann, G.A., Mazarico, E., Lemoine, F.G., Head III, J.W., et al., 2017. Summary of the results from the Lunar Orbiter Laser Altimeter after seven years in lunar orbit. Icarus 283, 70–91. https://doi.org/10.1016/j.icarus.2016.06.006.

Smith, W.H.F., Wessel, P., 1990. Gridding with continuous curvature splines in tension. Geophysics 55 (3), 293–305. https://doi.org/10.1190/1.1442837.

Speyerer, E.J., Lawrence, S.J., Stopar, J.D., Gläser, P., Robinson, M.S., 2016. Optimized traverse planning for future polar prospectors based on lunar topography. Icarus 273, 337–345. https://doi.org/10.1016/j.icarus.2016.03.011.

Wagner, R.V., Nelson, D.M., Plescia, J.B., Robinson, M.S., Speyerer, E.J., Mazarico, E., et al., 2017. Coordinates of anthropogenic features on the Moon. Icarus 283, 92–103. https://doi.org/10.1016/j.icarus.2016.05.011.

Watkins, R.N., Joliff, B.L., Mistick, K., Fogerty, C., Lawrence, S.J., Singer, K.N., Ghent, R.R., 2019. Boulder distributions around young, small lunar impact craters and implications for regolith production rates and landing site safety. J. Geophys. Res.: Plan 124, 2754–2771. https://doi.org/10.1029/2019JE005963.

Watson, K., Murray, B., Brown, H., 1961. On the possible presence of ice on the Moon. J. Geophys. Res. 66 (5), 1598–1600. https://doi.org/10.1029/JZ066i005p01598.

Wessel, P., Smith, W.H.F., Scharroo, R., Luis, J., Wobbe, F., 2013. Generic mapping Tools: improved version released. EOS Trans. AGU 94 (45), 409–410. https://doi.org/10.1002/2013EO450001.

Williams, J.G., Boggs, D.H., Folkner, W.F., 2008. DE421 Lunar Orbit, Physical Librations, and Surface Coordinates, 335–. IOM. JW,DB,WF-20080314-001, March 14, 2008.